Energetics of spreading droplets and role of capillary waves at low Weber numbers below 10

Ikroh Yoon, Jalel Chergui, Damir Juric, Seungwon Shin

Energetics of spreading droplets and role of capillary waves at low Weber numbers below 10

Ikroh Yoon (윤익로)[1], Jalel Chergui[2], Damir Juric[2,3] and Seungwon Shin (신승원)[4,a]

[1]Korea Institute of Marine Science and Technology Promotion (KIMST), Seoul, 06775 Korea (currently works at Intergovernmental Oceanographic Commission of United Nations Educational, Scientific and Cultural Organization), iryoon@kimst.re.kr

[2]Centre National de la Recherche Scientifique (CNRS), Laboratoire Interdisciplinaire des Sciences du Numérique (LISN), Université Paris Saclay, 91400 Orsay, France, Damir.Juric@lisn.fr, Jalel.Chergui@lisn.fr

[3]Department of Applied Mathematics and Theoretical Physics, University of Cambridge, Centre for Mathematical Sciences, Wilberforce Road, Cambridge CB3 0WA, UK

[4]Department of Mechanical and System Design Engineering, Hongik University, Seoul, 04066 Korea, sshin@hongik.ac.kr

[a)] Corresponding Author:
Professor Seungwon Shin, PhD
Phone: 82-2-320-3038
FAX: 82-2-322-7003
E-Mail: sshin@hongik.ac.kr

ABSTRACT

In this study, we investigate the energy conversion and dissipation mechanisms of spreading droplets on a solid surface at a low Weber number regime, which neither conventional energy-balance-based theories nor empirical scaling laws can completely explain. The energetic analysis presented in this study shows that on a hydrophilic surface, the actual primary energy source driving the spreading process is the initial surface energy not the initial kinetic energy. The conventional energy-balance-based approaches are found to be valid only for the spreading process on a hydrophobic surface. Particular attention is also paid to the roles of the capillary waves. The capillary waves are found to play significant roles in all of the important flow physics, i.e., the interfacial structure, the oscillatory motions and the rapid collapse of the liquid film, the onset of the viscous regime, and the energy loss mechanism. It is also shown that the energy dissipation caused by the capillary-wave-induced phenomena can be estimated to be 25-35% and 55-65% of the total energy loss for a hydrophilic and a hydrophobic surface, respectively, at the low Weber number regime.

Keywords: droplet impact; capillary wave; energetic analysis; multiphase flow; numerical simulation

I. INTRODUCTION

Droplet collision on a solid surface is a ubiquitous phenomenon which is very frequently observed in our everyday life (e.g., raindrops falling on an umbrella or a plant leaf) and various engineering applications such as inkjet printing [1], medical diagnostics [2], forensic analysis [3], agricultural sprays [4], self-cleaning surfaces [5], spray drying [6], spray cooling and chilling [7] and so forth. This fascinating phenomenon is also widely applied not only to diverse chemical engineering processes, e.g., fluid catalytic cracking (FCC) [8] or trickle-bed reactors [9], but also to many encapsulation technologies [10].

The dynamics during the spreading process of a droplet is governed by a complicated interplay among inertial, viscous, capillary, and gravitational forces [11-14]. Characteristic length and time scales are small [15] and continue to change over time and space [16,17]. In general, when the inertial force is sufficiently high enough to overwhelm the cohesion force, a droplet can splash on a solid surface generating several satellite droplets [11-14]. Below the splashing threshold [18], on the other hand, a droplet can be either gently deposited or (partially or completely) rebounded on a target surface depending on surface wettability [11-14]. The spreading process for common droplet impacts at relatively high impact speed is generally driven by inertial forces but limited by either capillary effects or viscous damping [19,20]. For some applications such as inkjet printing, however, a droplet can collide onto a target at a very low impact speed (low impact Weber number) where the Weber number is on the order of $O(10^0)$ to precisely control the quality of deposition [21]. In addition, in digital micro-fabrication technology, a molten liquid droplet can often undergo low speed impact to ensure a precise deposition on three-dimensional micro-structures [22]. In such collision cases, at low Weber number, the capillary effects and associated phenomena play dominant roles in spreading dynamics [23].

Numerous attempts have been made to understand the complex physical phenomena arising from droplet-solid interaction. Among others, many theoretical energetic studies, normally assisted by experiments, have been devoted to understanding the internal physics of droplets. The pioneering work of Chandra and Avedisian [24] has triggered a series of theoretical approaches based on the energy balance of a spreading droplet, which have been utilized as a powerful tool in recent decades to grasp the underlying physics for the spreading process. Under the assumption that the energy loss (i.e., viscous dissipation) occurs in the entire domain inside the droplet, Chandra and Avedisian [24] evaluated the magnitude of viscous dissipation and formulated an energy balance equation for the maximum spreading of the droplet. Afterward, many efforts have been made to better understand the droplet's energy conversion process and energy loss mechanisms. Pasandideh-Fard *et al*. [25] proposed new time and length scales to more realistically evaluate the time and volume (based on the boundary layer thickness) where the energy loss occurs. Based on Pasandideh-Fard *et al*.'s model [25], Mao *et al*. [26] proposed a semi-empirical model to cover a wide range of liquid viscosity and their model showed good agreement with many existing experimental data. Ukiwe and Kwok [27] and Wang *et al*. [28] also proposed new energetic models to more accurately represent surface energy at the maximum spreading state. They considered the circular ridge [27] and the rim-lamella shape [28] of droplets. Roisman [29] presented a remarkable analytical work which satisfies the full Navier-Stokes equations to evaluate the flow field and the energy loss in the boundary layer in more detail. They also proposed a semi-empirical correlation based on their theoretical analysis and experimentally fitted data, which has also been experimentally shown to be one of the most accurate representations of the spreading extent [17]. Wilderman *et al*. [30] presented an interesting interpretation of the energy balance during high speed impact of droplets. They considered various energy loss mechanisms during the spreading process and showed that roughly one-half of the initial

impact kinetic energy is transformed into surface energy due to a universal 'head loss', regardless of collision conditions and specific energy loss mechanisms. Huang and Chen [31] also showed an interesting energetic analysis of the droplet's spreading behavior, focusing on the energy loss mechanism during spontaneous wetting (so called 'interface relaxation'), and proposed an auxiliary dissipation to account for the contribution to the total energy loss for low speed impact problems.

There have also been several attempts to better evaluate the time scale for which a droplet spreads over a solid surface, i.e., the time at which the energy loss occurs (the so-called 'spreading time'). Lee *et al*. [32] rescaled the spreading time using the maximum spreading diameter and surface tension coefficient of water to consider the effect of surface tension on the time scale that energy loss takes place. Lin *et al*. [33] and Du *et al*. [34] also proposed an improved representation of the spreading time, as a function of Weber number. More recently, Aksoy *et al*. [35] and Xu *et al*. [36] refined the spreading time as a function of both Weber and Reynolds number to include the effect of liquid viscosity.

Scaling laws are more empirical compared to theoretical analyses, but provide very useful tools to understand the spreading characteristics. Scheller and Bousfield [37] proposed a correlation for the maximum spreading of droplets as a function of Weber and Ohnesorge number. Clanet *et al*. [19] presented their well-known scaling laws, i.e., the maximum spreading can be scaled by $We^{0.25}$ and $Re^{0.2}$ for the capillary-limited and viscous-limited regime, respectively. Lann *et al*. [38] proposed a new empirical relation which is a broad cross-over between two regimes (i.e., from low- to high- impact velocity regimes) by interpolating two scaling laws ($We^{0.5}$ and $Re^{0.2}$). Recently, Yoon and Shin [39] also proposed empirical scaling laws for the maximum spreading of droplets which can be applied to both flat and curved surfaces.

All these achievements reviewed above provide excellent insights which are of great help

in understanding the fundamental physics during the spreading process, and also can reproduce many experimentally observed spreading behaviors (e.g., the maximum spreading of droplets). However, as experimentally shown by Antonini *et al*. [17] and Lann *et al*. [38], the spreading behavior cannot yet be completely expressed well by a single representation for a broad range of collision conditions. Indeed, there still exist significant inconsistencies among many theoretical and empirical results. For example, some models for the maximum spreading [24-28,30,31] include the effect of surface wettability whereas some others [19,29,37-39] exclude it. In addition, for energy-balance-based approaches, various contact angles, e.g., static or equilibrium contact angles [26,40], advancing contact angle [27], or contact angle at the maximum spreading state [25], have been used to account for the surface wettability. It is therefore difficult to find a consensus among the model approaches and conclusions. For scaling laws, on the other hand, energy conservation and momentum conservation provide different scaling results for the maximum spreading of a droplet in the capillary regime, i.e., $We^{0.5}$ (from energy conservation) [41] and $We^{0.25}$ (from momentum conservation) [19]. In the viscous regime, energy conservation between kinetic energy and viscous dissipation yields $Re^{0.2}$ [42] whereas conservation between kinetic and surface energy before collision and surface energy and viscous dissipation at the maximum spreading state yields $Re^{0.25}$ [25]. Lann *et al*. [38] also experimentally showed that none of the various scaling laws ($We^{0.5}$, $We^{0.25}$, $Re^{0.25}$, and $Re^{0.2}$) holds for a wide range of liquid properties. All these inconsistencies mentioned above signify that our understanding of spreading behavior and the associated physics is still unclear in spite of the various existing studies in the context of both theoretical and empirical approaches.

In particular, we take note of the fact that a droplet can spread over a solid surface by purely capillary effects acting on the contact line, even in cases where the initial impact kinetic energy is very low (or even zero). For example, it has been experimentally [43] and numerically

[23] shown that the maximum spreading of a millimetric droplet can reach above its initial droplet diameter measured before contact [23,43], although the initial impact velocity is zero. This spreading phenomena without impact kinetic energy is called spontaneous spreading [28,31,40]. There must also be energy dissipation even for the case of spontaneous spreading due to motion of the droplet [31,40].

Such spreading phenomena at low impact kinetic energy (i.e., low Weber number) cannot be explained well by either conventional energy-balance-based theoretical approaches or existing scaling laws. In fact, if the initial impact velocity of a droplet approaches zero, most of the scaling laws (and empirical models) [19,29,37-39] converge to a zero value for the maximum spreading diameter (therefore yielding a zero value for the maximum spreading extent under zero impact velocity), which is physically impossible [43]. In addition, since most of the energy-balance-based theories [24-27,33,34,44] are also based on the assumption that the initial impact kinetic energy drives the spreading process and is transformed into surface energy or viscous dissipation, such a capillary-driven spreading behavior for low Weber number (including spontaneous spreading) cannot be explained well by those theories. More specifically, most energy-balance-based theories [24-27,33,34,44] also converge to a zero value of energy loss during the spreading process if the impact velocity approaches zero (in this case, the maximum spreading of the droplet is determined by a function of only surface wettability) because they consider the energy loss mechanism to be the viscous dissipation in the thin boundary layer and characterize the amount of energy loss using the Reynolds number. This result as well is physically unrealistic.

What is the actual potential energy driving the spreading process at low (or zero) impact kinetic energy (i.e., at a low Weber number regime)? It is evidently the surface energy associated capillary effects on a solid surface. In this context, one can find significant knowledge gaps in the above literature, which can be summarized as follows:

(i) The detailed changes in energy components and the primary energy source for driving the spreading process in the low Weber number regime are still unclear. To the best of our knowledge, surface energy has not been highlighted as a primary energy source even though it is obviously the major driving energy source for low speed impact problems (or spontaneous spreading).

(ii) Energy loss mechanisms for droplet impact at low Weber number are also still unclear, because most of the existing studies have mainly focused on viscous dissipation in the thin boundary layer. Although a few numerical studies have recently shed light on some other causes of energy dissipation, e.g., dissipation due to bubble entrapment and escape [45], residual kinetic energy [46], dissipation in the thin layer near a solid surface caused by spontaneous spreading [31], it still remains difficult to understand how the droplet's energy is dissipated during capillary-driven spreading in the low Weber number regime.

In this study, we present an energetic analysis of spreading droplets at low Weber number which cannot be explained by either conventional energy-balance-based theories or empirical scaling laws. Based on our detailed numerical simulations, changes of the energy budget and flow structure during the capillary-driven spreading process are captured in detail. In addition, particular attention is paid to the capillary waves, which demonstrate a significant role in the flow physics and energy loss mechanisms. Quantitative analysis of the energy loss caused by the capillary waves is also presented. To the best of our knowledge, this study is the first attempt not only to explain changes in the energy budget, considering surface energy as a primary energy source for driving the capillary-driven spreading process, but also to quantify energy loss caused by capillary-wave-induced phenomena.

II. SIMULATION METHOD

A. Numerical method

Since the current study aims at understanding the physical behavior of a spreading droplet in the low Weber number regime, our existing numerical setup remains predominantly intact. In this section, therefore, a brief introduction of our simulation methods is given rather than a fully detailed description. Readers can refer to our previous studies for more detailed information on our numerical formulations [23,39,47,48] and method validation.

For incompressible flow, the governing equations that are applied to both the liquid and gas phases and that are solved on a fixed Cartesian grid (Eulerian grid) are based on a single-field formulation:

$$\nabla \cdot \mathbf{u} = 0 \tag{1}$$

$$\rho\left[\frac{\partial \mathbf{u}}{\partial t} + \mathbf{u}\cdot\nabla\mathbf{u}\right] = -\nabla P + \rho\mathbf{g} + \nabla\cdot\mu\left(\nabla\mathbf{u} + \nabla\mathbf{u}^{\mathrm{T}}\right) + \mathbf{F} \tag{2}$$

where $\mathbf{u}$ and P are the velocity vector and the pressure, respectively, and $\mathbf{g}$ is the gravitational acceleration. ρ and μ are the density and viscosity, respectively. $\mathbf{F}$ is the surface tension force which is considered only at the phase (liquid–gas) interface, and can be represented by using the following continuum surface force (CSF) [49,50] formulation:

$$\mathbf{F} = \sigma\kappa_{\mathrm{H}}\nabla I \tag{3}$$

where σ is the surface tension coefficient. κ_{H} is the curvature of the interface and can be computed as follows:

$$\kappa_{\mathrm{H}} = \frac{\mathbf{F}_{\mathrm{L}} \cdot \mathbf{G}}{\mathbf{G} \cdot \mathbf{G}} \tag{4}$$

$$\mathbf{F}_{\mathrm{L}} = \int_{\Gamma(t)} \kappa_{\mathrm{f}} \mathbf{n}_{\mathrm{f}} \delta\left(\mathbf{x} - \mathbf{x}_{\mathrm{f}}\right) \mathrm{d}s \tag{5}$$

$$\mathbf{G} = \int_{\Gamma(t)} \mathbf{n}_{\mathrm{f}} \delta\left(\mathbf{x} - \mathbf{x}_{\mathrm{f}}\right) \mathrm{d}s \tag{6}$$

Here, $\mathbf{x}_{\mathrm{f}}$ is the position of the liquid-gas interface $\Gamma(t)$. The line integrals (or surface integrals in 3D simulations) are evaluated over a line element, ds, (or area element in 3D). κ_{f} is the interface curvature directly obtained from the Lagrangian interface. $\mathbf{n}_{\mathrm{f}}$ is the unit normal vector and $\delta(\mathbf{x}\text{-}\mathbf{x}_{\mathrm{f}})$ is the Dirac delta distribution function. Note that $\delta(\mathbf{x}\text{-}\mathbf{x}_{\mathrm{f}})$ has a non-zero value only at the interface ($\mathbf{x} = \mathbf{x}_{\mathrm{f}}$).

The physical properties (density and viscosity) of each phase (liquid and gas) denoted as b can be described using an indicator function I which has the characteristics of the Heaviside function and varies from zero (0) in one phase (liquid) to one (1) in the other phase (gas):

$$b = b_{\mathrm{d}} + \left(b_{\mathrm{a}} - b_{\mathrm{d}}\right) I \tag{7}$$

where the subscripts d and a denote the droplet (liquid) and air (gas), respectively.

As an interface method, the level contour reconstruction method (LCRM) [51-53] is used to represent the liquid-gas interfacial boundary. The LCRM is a hybridization of two well-established interface methods, i.e., front tracking [49,54] and level set [55]. In the LCRM, Lagrangian marker elements are tracked to accurately represent the phase interface (as in the

original front tracking method) but are reconstructed by using the distance function which provides level set characteristics. This hybridization allows us to avoid the 'logical connectivity' which is the most well-known drawback of the original front tracking method. Because the reconstruction procedure is performed on each cell-face on the Cartesian (Eulerian) grid, every Lagrangian marker element (i.e., line in 2D and triangle in 3D simulations) can be naturally (implicitly) connected, thus even highly dynamic interfaces do not require complex algorithmic treatment for topological changes of the interface.

The positions of the interfacial elements ($\mathbf{x}_f$) are advected in time with the interfacial velocity $\mathbf{u}_f$, by the second-order Runge-Kutta method. For elements which are not located on the contact line, $\mathbf{u}_f$ is directly obtained by interpolating the velocity field. On the other hand, for elements which are in contact with a surface, i.e., contact line elements, their velocity is determined by the Navier-slip condition to avoid a stress singularity. In this case, the contact line velocity (U_{CL}) is computed as $U_{CL} = \lambda(\partial\mathbf{u}/\partial\mathbf{n})_{wall}$, where $\partial\mathbf{u}/\partial\mathbf{n}$ is the shear strain rate on the wall. For the proportionality slip constant λ, we used the formerly validated value [53], i.e., a quarter of the grid size.

To consider contact angle hysteresis, the dynamic contact angle (θ_{dyn}) is modeled as a function of the equilibrium contact angle (θ_{eqi}) and the contact line velocity as follows [56]:

$$\theta_{dyn}\left(U_{CL}\right) = \begin{cases} \min\left[\theta_{eqi} + \left(\dfrac{Ca}{q_1}\right)^{1/3},\ \theta_{mda}\right], & \text{if } U_{CL} \geq 0 \text{ (for spreading)} \\ \max\left[\theta_{eqi} + \left(\dfrac{Ca}{q_2}\right)^{1/3},\ \theta_{mdr}\right], & \text{if } U_{CL} \leq 0 \text{ (for receding).} \end{cases} \tag{8}$$

where the capillary number Ca is defined as $Ca = \mu U_{CL}/\sigma$. θ_{mda} is the maximum advancing contact angle and θ_{mdr} is the minimum receding contact angle. q_1 and q_2 are experimentally

determined constants in relation with the surface conditions, and the same values as Yokoi *et al.* [56] are applied in the present study ($q_1 = 9.0 \times 10^{-9}$ and $q_2 = 9.0 \times 10^{-8}$). Note also that in the current study, the contact angle hysteresis is set to ±2.5°, because it is assumed that the solid surface is well-prepared [39].

Fig.1 illustrates the computational geometry with boundary conditions applied in this study. A two-dimensional axi-symmetric simulation is considered in order to reduce the required numerical resources. Note that the droplet impact behavior would be essentially identical to that from full three-dimensional simulations in the low Weber number regime [57], since there are no meaningful changes in flow structure in the circumferential direction (e.g., cusps or fingering [11-12]), which are generally observed during collisions at high Weber number (e.g., splashing phenomena). The lengths of the simulation domain in the axial (z) and radial (r) directions are set as $Z_L = 7.5D_d$ and $R_L = 10D_d$, respectively, where D_d denotes the diameter of the droplet. Open boundary conditions are applied to the upper and right boundaries, whereas a solid wall boundary condition is applied to the lower boundary. An axi-symmetric boundary condition is applied to the left boundary. Before the collision with a target, the droplet is artificially accelerated by using an enhanced gravity field to ensure that the initial impact velocity reaches a predetermined velocity value. The effects of initial deformation before the impact and turbulence are not considered, owing to their negligible effects [58].

Note that the numerical framework described herein has been utilized in our various previous studies on droplet collision problems, and has also been thoroughly validated by comparisons with diverse experimental works for a wide range of impact conditions including at low Weber number [23,47,48]. More detailed information on our simulation methods, e.g., the advection of the phase interface, the reconstruction of Lagrangian interface elements, and other simulation techniques can also be found in [23,39,47,48].

B. Computation of energy components

A common approach [39,59] is used to calculate each energy component of the droplet, i.e., the kinetic energy (E_k), the gravitational energy (E_g), the surface energy (E_s), and the viscous dissipation (E_d). The kinetic (E_k) and gravitational energy (E_g) can be obtained as:

$$E_k = \frac{1}{2}\rho_d \int_\Lambda \left(u_r^2 + u_z^2\right) d\Lambda \tag{9}$$

$$E_g = \rho_d \Lambda g z_d \tag{10}$$

Here, Λ and z_d denote the volume and the volumetric centroid of the droplet, respectively. The surface energy E_s is calculated as:

$$E_s = \sigma\left[A_{LG} - A_{LS}\cos\theta_{eqi}\right] \tag{11}$$

Here, A_{LG} and A_{LS} are the liquid-gas interfacial area and the liquid-solid contact area (i.e., wetted area), respectively. Therefore, the first term (σA_{LG}) in Eq.(11) denotes the liquid-gas interfacial surface energy, whereas the second term ($\sigma A_{LS}\cdot\cos\theta_{eqi}$) accounts for the capillary effect on the liquid-solid contact area, which is essentially a function of the surface wettability and the wetted area.

The viscous dissipation E_d is calculated as:

$$E_d = \int_0^t \left(\int_\Lambda \Phi \, d\Lambda\right) dt \tag{12}$$

where the dissipation function Φ is:

$$\Phi = 2\mu_{\mathrm{d}}\left[\left(\frac{\partial u_r}{\partial r}\right)^2+\left(\frac{u_r}{r}\right)^2+\left(\frac{\partial u_z}{\partial z}\right)^2+\frac{1}{2}\left(\frac{\partial u_r}{\partial z}+\frac{\partial u_z}{\partial r}\right)^2\right] \tag{13}$$

Note that the calculations of z_{d}, A_{LG}, and A_{LS} are very straightforward since the liquid-gas interface and the location of the contact line are explicitly tracked using the Lagrangian elements. Note also that this approach was validated in our previous study [39] by a comparison with an existing study [30].

III. RESULTS AND DISCUSSION

A. Validations

In this subsection, we validate our numerical method for simulating droplet spreading problems in the low Weber number regime. Since the spreading process is significantly affected by surface wettability and the associated capillary effect at low Weber number, our benchmark test results are compared to existing experimental results for three different surface wettabilities (i.e., hydrophilic, neutral, and hydrophobic surfaces). Note that water droplets are considered for its versatility for all simulation cases considered in this paper. Therefore, the density and the viscosity of the droplet are set as $\rho_{\mathrm{d}} = 998.2$ kg/m^3 and $\mu_{\mathrm{a}} = 0.001$ N s/m^2, respectively. The surface tension coefficient is set to be $\sigma = 0.0728$ N/m.

In Fig.2(a), the temporal variations of the nondimensional spreading diameter β^* ($\beta^* = \beta/D_{\mathrm{d}}$, where β is the contact diameter between the droplet and the solid surface) for three different grid resolutions are depicted. All simulation conditions are the same as in the existing experiment of Lee *et al*. [43], i.e., the surface wettability is hydrophilic (steel, $\theta_{\mathrm{eqi}} = 61°$) and the initial impact velocity (V_{ini}) is set as zero (i.e., the spreading process is completely driven by the capillary effect without impact kinetic energy). The diameter of the droplet is set as D_{d}

= 2 mm. The inset in Fig.2(a) shows the interfacial morphologies at $t = 0.02$ s obtained by using the three different grid resolutions. As can be seen, mesh convergence is almost achieved at 32 CPR (cells per radius of droplet) in terms of both qualitative and quantitative measurement, and the maximum value of β^* is consistent with the previous experimental result [marked by a black cross in Fig.2(a)] [43]. Note that in the present study, to be on the safe side, a grid resolution of 64 CPR is applied to all later simulation cases.

In Fig.2(b), we compare the temporal variation of β^* with the experimental result of Huang and Chen [31] for a hydrophobic surface (parafilm, $\theta_{eqi} = 110°$). The diameter of the droplet and the impact velocity are $D_d = 2.7$ mm and $V_{ini} = 0.49$ m/s, respectively. The corresponding Weber number ($We = \rho_d V_{ini}^2 D_d/\sigma$) is We = 8.9. Three insets in Fig.2(b) compare the simulated droplet's interfacial morphologies with the experimental observations at $t = 0.97$, 1.98, and 4.75 s. As shown, our simulation result shows good agreement with the existing experimental result [31].

In Fig.2(c), we further validate our simulation capability by a comparison of the nondimensional film thickness h^* ($h^* = h/D_d$, where h is the height of the liquid film measured at the collision center) with the experimental result of Mitra *et al*. [60], for a neutral surface (brass, $\theta_{eqi} = 86°$). Note that experimental data for the temporal evolution of the film thickness on a flat substrate at this low We regime are very rare since it is a difficult quantity to precisely measure in the experiment, owing to the limited camera-based measurements (viewing the central area of the droplet is usually obscured by the outer rim due to its concave shape at the central region) [61]. Therefore, quantitative analysis of the film thickness has been mainly carried out on curved surfaces (e.g., on a particle) in experimental studies [60-62]. We also consider here the droplet impact on a spherical particle using the same numerical formulation described in the above section to compare our simulated h^* with the existing experiment. Fig.2(c) depicts the temporal evolution of h^* on the brass particle which has a diameter of 3

mm. The diameter of the droplet and the impact velocity are set as D_d = 2.61 mm and V_{ini} = 0.73 m/s, respectively, thus the corresponding Weber number is We = 19.1. As seen in the figure, our simulation result again shows good agreement with the existing experimental result [60]. From our benchmark tests shown in Fig.2, we concluded that our numerical methods can reasonably simulate the spreading phenomena of droplets on various solid surfaces, from hydrophilic to hydrophobic, in the context of both qualitative and quantitative comparisons. Note also that our simulation methods used herein have been extensively and thoroughly validated by comparisons with many experimental works [23,39,47,48] including low Weber number collision cases [23,47,48].

B. Capillary wave driven spreading and flow characteristics

Based on our validated computational framework above, in this subsection, we examine the spreading behavior and flow characteristics for two different surfaces wettabilities, i.e., hydrophilic (θ_{eqi} = 20°) and hydrophobic surfaces (θ_{eqi} = 125°), and present the significant role of the capillary waves in more detail. To observe the typical spreading characteristics in the low Weber number regime, in the following numerical simulations the diameter of the droplet (D_d) and the impact velocity (V_{ini}) are set as D_d = 2 mm and V_{ini} = 0.355 m/s, respectively, thus the corresponding Weber number is We = 3.5. The time is now also non-dimensionalised using the capillary-inertial time scale $t_c = (\rho D_d^3/8\sigma)^{0.5}$, and the non-dimensional capillary-inertial time τ is defined as $\tau = t / t_c$ hereafter, unless otherwise mentioned.

Fig.3 depicts the droplet's morphologies and velocity vectors, on the hydrophilic surface during the spreading process. At a very early stage of spreading [Fig.3(a)], the bottom part of the droplet is squeezed, and a capillary wave starts to be formed above the contact line. Afterward, the droplet quickly spreads and wets the solid surface owing to its strong wetting nature and low equilibrium contact angle on the hydrophilic surface [Fig.3(b)]. Since the

contact line moves faster than the upper part of the droplet, the valley (trough) of the capillary wave is clearly formed above the contact line [see black arrow in Fig.3(b)]. As the contact line moves outward, the gradient of local curvature along the liquid-gas interface increases [63,64], and the contact line acts like a moving wave source [65]. These waves generated in the vicinity of the contact line are propagated to the top part of the droplet along the liquid-gas interface, leading to the interfacial shape captured in Fig.3(c) [31,63]. Such an interfacial structure caused by the capillary waves is called a 'pyramidal structure' showing a staircase-like shape [46] [see black arrow in Fig.3(c)]. Note that this pyramidal structure has also been observed in other previous experiments and simulations at similar impact conditions (We ~ 4 - 5) on both hydrophilic and hydrophobic surfaces [25,46]. At this time, strong redirections of the liquid flow are seen inside the droplet near the valley of the capillary wave, whereas vortical motions of the gas flow are observed outside the interface. The traveling waves encounter each other at the central top part of the droplet, resulting in oscillatory motion of the top part due to wave interference [31]. The increased downward velocity vectors resulting from the first oscillation are depicted in the zoom-in of the dashed red box of Fig.3(c). Note that the velocities of these downward flows are much faster than the initial impact velocity [compare the sizes of velocity vectors between Fig.3(a) and Fig.3(c)]. The top part of the droplet rises again due to its second oscillatory motion, and the upward flow with locally induced vortical motions are captured in the zoom-in of the dashed red box of Fig.3(d). The third oscillatory motion at the central top part leads to the rapid collapsing of the liquid film [33,63], and a strong downward flow is observed during this collapse, as depicted in Fig.3(e). Since the liquid film at the collision center is drastically thinned due to this rapid collapse, the central top part of the liquid film encounters the growing boundary layer from the solid surface. Therefore, the liquid flow inside the droplet enters the viscous regime [61,62] and the droplet starts to be considerably affected by viscous damping. After this moment, the change in the liquid film thickness becomes

minimized, and is almost kept at a very thin level (we will discuss the growth of the boundary layer and entry into the viscous regime in detail later). At the maximum spreading state, the droplet forms a toroidal shape with a thin center, as shown in Fig.3(f). Note that the retraction process is not fully demonstrated since here we mainly focus on the spreading stage (i.e., the recoiling motion is beyond the current scope).

Fig.4 shows the case for the hydrophobic surface. At a very early stage of the spreading process [Fig.4(a)], similar behaviors to those for the hydrophilic surface (i.e., the squeezed bottom part of the droplet and the formation of waves) are observed near the contact line. However, unlike where a valley of the wave is developed above the contact line for the hydrophilic surface, a peak (crest) of the wave is observed [see black arrow in Fig.4(b)], due to the slow motion of the contact line and the non-wetting nature of the hydrophobic surface. Since the capillary waves are primarily generated by the difference between the equilibrium contact angle and the apparent contact angle at the initial stage, the hydrophobic surface provides relatively reduced local interface curvature near the contact line and weaker waves [64,65] compared to the hydrophilic surface. Therefore, the interfacial shape is relatively rounded in the vicinity of the contact line, and the staircase-like structure is much more smoothed [see black arrow in Fig.4(c)]. In Fig.4(c) and (d), the first (downward) and second (upward) oscillatory motions are also observed, respectively, as depicted in the zoom-in of the dashed red boxes. The third oscillation and induced rapid collapse of the central top part are also captured in Fig.4(e). However, its deformation is relatively less severe due to the weaker capillary waves and smoothed staircase-like structure, which eventually leads to weaker downward fluid motion compared to that on the hydrophilic surface. Even though the liquid film is rapidly collapsing, its thickness is still sufficiently thick compared to the boundary layer thickness [Fig.4(f)], thus the droplet cannot enter the viscous regime. Therefore, the central top part of the droplet (and its film thickness) rises up again at the subsequent stage, without notable

viscous resistance (the detailed rising motion is not demonstrated here but will be discussed later). At the maximum spreading state, the droplet forms a toroidal shape with a thicker center [Fig.4(f)].

In order to examine in more detail the dependence of different characteristics of the capillary waves on surface wettability, the time-dependent wave propagation behavior is quantitatively compared in Fig.5. The capillary waves of the droplet at given time instants can be characterized by the radius of the deformed droplet interface r_w, as illustrated in Fig.5(a). The point C can be regarded as the moving reference point for measuring r_w, and the position of C is updated ensuring that the distance between the point C and the central top part of the droplet (point A) is always kept as the initial droplet radius r_d. ψ denotes the angle between the axis of symmetry and the position vector of r_w. Fig.5(b) and (c) depict the propagation of the capillary waves for the hydrophilic and hydrophobic surfaces shown in Fig.3 and Fig.4, respectively. The time-dependent angular distributions of r_w (normalized by r_d) are compared in detail. For both surfaces, as seen, the amplitudes of the waves globally increase as the droplets spread over the surfaces. However, the amplitudes on the hydrophilic surface at given time instants are roughly double those on the hydrophobic surface, signifying that the capillary waves are much stronger on the hydrophilic surface. In addition, on the hydrophilic surface, the valley of the capillary wave is formed near the contact line [left side of the contact line in Fig.5(b)] as shown above in Fig.3. Conversely, the peak of the wave and the rounded shape are observed near the contact line on the hydrophobic surface.

Fig.6 quantitatively analyses the temporal variations of the nondimensional film thickness (h^*) measured at the collision center for the two cases shown in Fig.3 and Fig.4. Note that in Fig. 6, a different time scale, i.e., the advective time scale ($t_a = D_d/V_{ini}$) is considered to compare our simulation results with the existing studies, and the non-dimensional advective time τ_a is denoted as $\tau_a = t / t_a$. If a droplet collides on a solid surface at a sufficiently high We, temporal

changes in h^* can be well described by the universal solutions [61,62]. During the first phase, the so-called 'initial drop deformation period', h^* is not affected by the presence of the solid surface and can be simply described as $h^* = 1 - \tau_a$. In this phase, the top part of the liquid film shows rigid-body-like motion [61,62]. Afterward, for the second phase, the so-called 'inertia dominated period', flow in the lamella far from the edge (i.e., far from the contact line) can be assumed to be mainly dominated by the inertial effect without notable viscous resistance, thus the internal liquid motion can be described by the inviscid solution which has the same form as the well-known far-field asymptotic solution [66]. During the second (inertia dominated) phase, h^* can be represented by the universal curve, i.e., $h^* = 0.39/(0.25+\tau_a)^2$ [61]. Note that these universal profiles have also been theoretically [61,62], experimentally [62], and numerically [48] confirmed. As examples, the temporal variations of h^* for 6 additional cases at the high We regime (We = 50, 70, and 90, and $\theta_{eqi} = 20°$ and 125°) are plotted together in Fig.6 (see black solid lines). As depicted in the zoom-in of the gray dashed box, it is clearly observed that h^* for all those high We cases collapse onto the two universal curves (green dashed lines) showing an excellent agreement with the existing studies [48,61,62].

For spreading at the low We regime, however, h^* can be represented by the universal solution only for the early stage of the first phase ($\tau_a \leq 0.4$), and h^* significantly diverges from the universal profiles (compare red and blue solid lines with the green dashed lines) after $\tau_a \sim 0.4$, because the motion of the liquid film is no longer governed by inertial effects but primarily dominated by the capillary waves, even in the central part of the droplet which is quite far from the contact line. Near $\tau_a \sim 0.4$, the oscillatory motions and the subsequent rapid collapsing of h^* are observed, resulting from the merging of the capillary waves at the central top part of the droplet (see the zoom-in of the orange dashed box). As already described in Figs.3 and 4 above, the collapse of h^* is more drastic on the hydrophilic surface ($\theta_{eqi} = 20°$) due to the stronger capillary waves. Note that the difference of h^* near the final stage depending on the surface

wettability (i.e., staying at minimal level on the hydrophilic surface whereas it rises again on the hydrophobic surface) is primarily determined by the onset of the viscous regime which is also dominated by the capillary waves and associated phenomena (i.e., how much the liquid film collapses due to the oscillatory motions).

C. Energetics of the spreading droplet : primary energy source for driving the spreading process

In section 3.B above, we have investigated the capillary-driven spreading behaviors and flow structures at low Weber number, and the dominant roles of the capillary waves depending on the surface wettability have been observed. During the entire spreading process, capillary waves have been found to play a significant role in determining the droplet's interfacial morphologies (e.g., staircase-like structures), the oscillatory motions of the central top part and its collapse, and the onset of the viscous regime. We now examine the energetics of the droplet, focusing on the changes in the energy components of the droplet in detail.

Fig.7 and Fig.8 depict the temporal changes in the energy components of the droplet for the two cases analyzed above (θ_{eqi} = 20° and 125°, We = 3.5). In Fig.7, the changes in all energy components are plotted together in the first subfigure [Fig.7(a)] whereas the changes in the kinetic energy (E_k), the surface energy (E_s), the cumulated viscous dissipation (E_d), and the gravitational energy (E_g) are separately plotted in the other subfigures [Fig.7(b-e)]. Note that the energy loss caused by contact angle hysteresis, which can be scaled as $\sigma D_m^2(\theta_{adv} - \theta_{rec})$ where D_m is the maximum spreading extent of droplets, can be negligible due to the low contact angle hysteresis considered herein (±2.5°). Each energy component is normalized by the initial kinetic energy $E_{k,ini}$, whereas the non-dimensional capillary-inertial time τ is rescaled by the maximum spreading time τ_{max} (therefore, $\tau / \tau_{max} = 1$ stands for the maximum spreading state). Note that the initial surface energy ($E_s / E_{k,ini}$) at the collision instant ($\tau / \tau_{max} = 0$) is more than

three times the initial kinetic energy (E_k / $E_{k,ini}$), meaning that surface energy can play a more dominant role in the spreading process than kinetic energy.

On the hydrophilic surface ($\theta_{eqi} = 20°$), since a decrease in the surface energy as the droplet spreads over a solid surface is energetically favorable [67], E_s / $E_{k,ini}$ naturally decreases during the spreading process. Basically, both the kinetic energy and the surface energy decrease until the droplet reaches the maximum spreading state (τ / $\tau_{max} = 1$), and they are all converted into viscous dissipation. It is interesting to observe that the kinetic energy even increases at the early stage of the spreading process [see τ / $\tau_{max} \leq 0.2$ in Fig.7(b)]. This indicates that the initial impact velocity is accelerated by the capillary effect acting in the vicinity of the contact line even after the collision instant. Note that this is contrary to the conventional assumption [24-27,33,34], which assumes that the initial kinetic energy is transformed into either surface energy or viscous dissipation. Such an energy transition from surface energy to kinetic energy highlights that the "real potential energy source (not meaning gravitational energy)" driving the spreading process on the hydrophilic surface is the initial surface energy not the initial kinetic energy. Since this energy transition from surface energy to kinetic energy occurs near a solid surface, a considerable part of the transformed kinetic energy is presumably dissipated by the strong viscous resistance from the surface. Although the detailed internal transition process (from surface energy to kinetic energy, and then eventually to viscous dissipation) cannot be explicitly captured because it occurs coincidently as well as implicitly, it is evident that surface energy is transformed into kinetic energy and finally dissipated by viscous resistance. The underlying physical mechanism driving the spreading process is the capillary effect acting near the contact line.

It is also observed that the kinetic energy quickly decreases near τ / $\tau_{max} = 0.62$, and the change in the surface energy is minimized after τ / $\tau_{max} = 0.62$ [see Figs.7(b) and (c)]. This is presumably caused by the onset of the viscous regime. After near τ / $\tau_{max} = 0.62$, the kinetic

energy is quickly dissipated whereas the changes in the surface energy are minimized. For this period, two different surface energy terms, i.e., the liquid-gas interfacial energy [σA_{LG} in Eq.(11)] and the capillary energy acting on the contact area [$\sigma A_{LS} \cdot \cos\theta_{eqi}$ in Eq.(11)], are almost counterbalanced. In other words, the liquid-gas interfacial energy continues to increase but the capillary energy gradually decreases until the droplet reaches the maximum spreading state (we will check that the onset of the viscous regime occurs near $\tau / \tau_{max} = 0.62$ later). Overall, at the maximum spreading state ($\tau / \tau_{max} = 1$), the total amount of the cumulated viscous dissipation $E_{d,max} / E_{k,ini}$ is 3.79, which is the same as the sum of the decrease in the surface energy [$(E_{s,ini} - E_{s,max})/E_{k,ini} = 2.68$], the decrease in the kinetic energy [$(E_{k,ini} - E_{k,max})/E_{k,ini} = 0.97$], and the decrease in the gravitational energy [$(E_{g,ini} - E_{g,max})/E_{k,ini} = 0.14$], where the subscript 'max' denotes the maximum spreading state. In other words, a total of $3.79 \times E_{k,ini}$ contributes to the spreading process and is dissipated, and a major contributor is apparently the surface energy ($2.68 \times E_{k,ini}$, about 70% of the total contribution).

Fig.8 depicts the case for the hydrophobic surface ($\theta_{eqi} = 125°$). As seen in Fig.8(a), $E_s / E_{k,ini}$ increases during the spreading process because reducing the surface energy as the droplet spreads over a solid surface is energetically unfavorable on the hydrophobic surface. For this case on the non-wettable surface, the only decreasing energy component is the kinetic energy (the gravitational energy also slightly decreases but its contribution is very minor). As seen, $E_k / E_{k,ini}$ continues to decrease until the maximum spreading state, and is converted into $E_s / E_{k,ini}$ and $E_d / E_{k,ini}$. Therefore, the conventional assumption that the initial kinetic energy drives the spreading process and is transformed into either the surface energy or the viscous dissipation is still valid for this non-wettable surface. At the maximum spreading state ($\tau / \tau_{max} = 1$), $E_d / E_{k,ini} = 0.34$, which is significantly less than the amount of energy dissipation on the hydrophilic surface (the energy dissipation and detailed mechanisms will be quantitatively analyzed later). Overall, at $\tau / \tau_{max} = 1$, the sum of the decrease in the kinetic energy [$(E_{k,ini} - E_{k,max})/E_{k,ini} =$

0.99] and the decrease in the gravitational energy [$(E_{g,ini} - E_{g,max})/E_{k,ini} = 0.11$] is the same as the sum of the increase in the surface energy [$(E_{s,max} - E_{s,ini})/E_{k,ini} = 0.76$] and the cumulated viscous dissipation ($E_{d,max} / E_{k,ini} = 0.34$). In other words, a total of $1.10 \times E_{k,ini}$ contributes to the spreading process and is dissipated, and a major contributor is obviously the kinetic energy ($0.99 \times E_{k,ini}$, about 90% of the total contribution).

Since the energy budget can provide useful insights and to understand changes in energy profiles more easily, in Fig.9 we re-draw the energy profiles analyzed above using the energy budget concept [30] to help understand how the droplet's initial driving energy sources are converted into other energy terms. For the hydrophilic surface, as shown in Fig.7 above, the primary energy source is the initial surface energy (about 70% of the total contribution) and it is transformed into kinetic energy by inducing liquid motion near the contact line. This increased kinetic energy is eventually dissipated by viscous dissipation. Therefore, in Fig.9(a), energy-variation quantities are now normalized by the total change in three energy sources [i.e., $\Delta E_t = \Delta E_k + \Delta E_s + \Delta E_g = (E_{k,ini} - E_{k,max}) + (E_{s,ini} - E_{s,max}) + (E_{g,ini} - E_{g,max})$] to include the surface energy as an energy source. E^*_k ($E^*_k = E_k / \Delta E_t$) and E^*_d ($E^*_d = E_d / \Delta E_t$) in Fig.9(a) denote the kinetic energy and the cumulated viscous dissipation normalized by ΔE_t, respectively, whereas the gravitational energy is not separately plotted for simplicity, owing to its minor role (its contribution is lumped into the kinetic energy). To clarify the physical interpretation of Fig.9(a), an example diagram is also added to the upper-right corner. Note that the regions above the black line (orange region in the example), below the blue line (blue region in the example), and between the black and blue lines (green region in the example) represent the budget of the kinetic energy, the viscous dissipation, and the surface energy, respectively. It is reasonable to understand the spreading process on the hydrophilic surface as one where the initial surface energy is transformed into kinetic energy and then this increased kinetic energy is eventually (and also coincidently) converted into viscous dissipation, driving the spreading process until

the flow enters the viscous regime [see τ / τ_{max} ~ 0.62 indicated by green dashed line in Fig.9(a)]. Note that the time for onset of the viscous regime is denoted by τ_{vis} hereafter. At $\tau = \tau_{vis}$, the droplet still has enough kinetic energy presumably resulting from the accelerated flow motions of the capillary effects and the rapid collapse of the central top part and induced flow motions, but which is quickly dissipated after τ_{vis}

Conversely, for the hydrophobic surface, the primary energy source is the initial kinetic energy (about 90% of the total contribution) and it is transformed into surface energy and viscous dissipation as shown in Fig.8. Therefore, energy-variation quantities can still be normalized by the initial kinetic energy, because it is the *de facto* unique energy source for the spreading process. ΔE^*_s [$\Delta E^*_s = (E_s - E_{s,ini}) / E_{k,ini}$] and E^*_d ($E^*_d = E_d / E_{k,ini}$) in Fig.9(b) denote the variation of surface energy and the cumulated viscous dissipation normalized by $E_{k,ini}$, respectively. Note that for the hydrophobic surface, the regions above the black line (green region in the example), below the blue line (blue region in the example), and between the black and blue lines (orange region in example) represent the budget of the surface energy, the viscous dissipation, and the kinetic energy, respectively. As seen, the initial kinetic energy drives the spreading motion, and about 70% of the initial kinetic energy is transformed into surface energy.

D. Energy loss mechanisms

In section 3.C above, we have investigated the overall changes in the energy components and the energy budgets for both the hydrophilic and the hydrophobic surfaces. We now examine the energy loss mechanisms for the spreading droplet at the low We regime in more detail.

For the hydrophilic case, in Fig.10, the spatial distributions of the viscous dissipation calculated from Eq.(13) are depicted at the left side of each panel, whereas interfacial morphologies and velocity vectors are shown in the right side of each panel. At the very early

stages, as seen, the energy dissipation mainly appears in the area where collision occurs and the liquid is squeezed [see Fig.10(a)]. As the capillary waves developed near the contact line are propagated to the top part of the droplet, the energy dissipation locally but strongly occurs where the gradient of interface curvature is high (i.e., near the valley of the wave) and the oscillation occurs (i.e., near the central top part) [see Fig.10(c-d)]. In particular, when the central top part is rapidly collapsed, significant dissipation is observed in almost the entire part of the central region [see Fig.10(e)]. At τ / τ_{max} = 0.62, as mentioned above, the liquid film is drastically thinned due to the rapid collapse, and the top part of the liquid film encounters the growing boundary layer [see Fig.10(f)], signifying the onset of the viscous regime [61,62]. Afterward, the flow inside the droplet is quickly dissipated by the viscous damping but the droplet can continue its spreading mainly due to the capillary effect. At the maximum spreading state, as the flow motions almost stop, energy dissipation disappears except for some parts near the solid surface [see Fig.10(g)]. Note that considerable viscous dissipation is observed near the solid wall during almost the entire spreading process because the capillary effect acting near the contact line continues inducing flow motion near the wall.

For the hydrophobic case, in Fig.11, the energy loss mechanisms are seen to be similar to those for the hydrophilic surface. The energy dissipation is observed mainly where the gradient of the interface curvature is high, where the oscillations and the induced rapid collapse occur, and near the solid wall. However, all of those contributions are obviously less than those for the hydrophilic surface and in particular, significantly reduced energy dissipation is observed near the solid wall compared to that on the hydrophilic surface due to the non-wettable nature of the hydrophobic surface (e.g., smaller wetting area and wetting velocity).

Overall, all the energy dissipation for both the hydrophilic and the hydrophobic surfaces are shown to be primarily caused by the two following mechanisms: (i) capillary-wave-induced dissipation (e.g., the flow redirections near the capillary waves, the induced oscillatory motions

of the interface and the rapid collapse of the liquid film) and (ii) the near-wall dissipation.

We now quantitatively compare the relative importance of those two energy loss mechanisms. Since it is reasonable to consider that the near-wall dissipation mainly occurs in the boundary layer [25], those two different dissipation quantities (i.e., capillary-wave-induced dissipation at the outer flow regime, and the near-wall dissipation in the boundary layer) can be spatially separated by the boundary layer. Indeed, an exact evaluation for the boundary layer thickness is very difficult owing to the complex flow structure inside the droplet (and is also beyond the current scope). Although some approximate values for the boundary layer thickness have been proposed as a constant value [25,34], those simple approximations are improper for this type of analysis because the boundary layer thickness varies considerably over time. Therefore, the time-dependent boundary layer thickness should be considered to separately quantify two different energy dissipation quantities. The boundary layer thickness as a function of time can be scaled as $\delta_{0.99} \sim \alpha(vt)^{0.5}$ where the numerical prefactor α has been proposed to be from 1.00 [41] to 1.88 [29].

Therefore, in Fig.12(a), we first plot the changes in two energy dissipation quantities for 4 different numerical prefactors i.e., α = 1.00, 1.88, 3.00 and 4.00. The energy dissipation at the outer flow region and the dissipation in the boundary layer are denoted as $E_{d,o}$ (blue lines) and $E_{d,i}$ (red lines), respectively, whereas the total dissipation (which is essentially the same as the sum of $E_{d,o}$ and $E_{d,i}$) is denoted as $E_{d,t}$ (black line). As seen, if α = 1.00, $E_{d,o}$ and $E_{d,i}$ show quite different profiles to the other cases (compare thick solid lines with the others). This means that there exist considerable changes in the flow motions across the estimated boundary layer, which is physically improper in the context of the definition of boundary layer. Since there is no notable difference in $E_{d,o}$ and $E_{d,i}$ for the other three cases (α = 1.88, 3.00, and 4.00), they all could be candidates for the approximation of boundary layer thickness. Here we choose the model of Roisman (α = 1.88) [29] since it was derived considering the full Navier-Stokes

equations.

Figs.12(b) and (c) depict the temporal variations of the nondimensional film thickness h^* shown in Fig.6 again, but now the time-dependent boundary layer thickness estimated by the chosen model is also plotted. Note that the boundary layer thickness is also nondimensionalized as $\delta^*_{0.99} \sim 1.88(\tau/\mathrm{Re})^{0.5}$. For the hydrophilic surface, as seen in Fig.12(b), since the rapid collapse of top liquid film occurs (see $0.4 \leq \tau / \tau_{max} \leq 0.6$) due to the capillary waves after the oscillatory motion of the central top part of the droplet, a large decrease in h^* is seen. After the onset of the viscous regime (τ_{vis}), however, the decrease in h^* is suddenly suppressed and the change in h^* is eventually minimized even after the maximum spreading state ($\tau / \tau_{max} > 1$) due to the significant viscous resistance. Note that h^* does not rise again despite its oscillatory nature and the surface tension force acting on the concave interfacial shape at the central part. Conversely, on the hydrophobic surface, the rapid collapse of the central part of the droplet is relatively less drastic compared to that on the hydrophilic surface, thus it doesn't encounter the boundary layer (the droplet cannot enter the viscous regime). As seen in Fig.12(c), h^* can start to rapidly rise again after the maximum spreading state ($\tau / \tau_{max} > 1$) without significant viscous resistance. From Fig.12, the estimated boundary layer thickness seems to reasonably explain the different physical behavior of the film thickness depending on the surface wettability.

To further visually validate our estimation of boundary layer thickness, in Fig.13, the viscous dissipation fields and the time-dependent growing boundary layer are compared together. As seen, the estimated boundary layer thickness (see yellow lines) can sharply separate those two flow regions, from the early collision stage [Fig.13(a)] to $\tau = \tau_{vis}$ [Fig.13(c)]. Overall, we conclude that our estimation of the time-dependent boundary layer thickness can spatially separate two flow regions (the outer flow region and the inner boundary layer) and the associated energy loss mechanisms (the capillary-wave-induced dissipation and the near-wall dissipation) well.

Based on the estimation of boundary layer thickness checked above, in Fig.14, the accumulated total energy dissipation $E_{d,t}$ is now separately quantified as (i) the capillary-wave-induced dissipation in the outer region (denoted by $E_{d,o}$), and (ii) the near-wall dissipation in the boundary layer (denoted by $E_{d,i}$). All dissipation quantities are normalized by the total energy dissipation at $\tau = \tau_{max}$. As seen in Fig.14(a), on the hydrophilic surface, about 70% of the total energy loss occurs in the boundary layer until $\tau = \tau_{max}$ (see red dotted line), signifying that the major energy loss mechanism is the near-wall dissipation. Note that after $\tau = \tau_{vis}$, no meaningful change in $E_{d,o}$ is observed because most parts of the entire flow field enter the viscous regime and the flow in the liquid film is mainly affected by considerable viscous damping. On the hydrophobic surface, conversely, the droplet cannot enter the viscous regime. In this case, the capillary-wave-induced dissipation continues to increase until $\tau = \tau_{max}$, and accounts for more than half (about 55%) of the total energy loss at $\tau = \tau_{max}$ [see blue dashed line in Fig.14(b)].

In Fig.15, we further examine the relative importance of two different energy loss mechanisms for a wider range of Weber number. Fig.15(a) and (b) depict the normalized $E_{d,o}$ for the hydrophilic and the hydrophobic surface, respectively, for a range of $1 \leq We \leq 10$. Note also that this range of Weber number has generally been known as the capillary-driven spreading regime [23]. As seen in Fig.15(a), $E_{d,o}$, the energy loss in the outer flow region primarily caused by the capillary waves, accounts for about 25-35% of the total energy loss for the hydrophilic surface. Conversely, on the hydrophobic surface, $E_{d,o}$ is kept at about 55-65% for a range of Weber number considered herein. We concluded that the major trends shown in Fig.14 above hold for the capillary-driven spreading regime [i.e., for a Weber number range on the order of $O(10^0)$].

Note also that if We further increases, the spreading dynamics and associated energy loss mechanism can significantly differ from those shown in Fig.15 [30,31,39]. For high speed

impact cases where the impact velocity is much higher than the velocity of the contact line, the flow physics is primarily dominated by the inertial force, whereas the role of surface wettability can usually be minor [19,20,30,39]. At an initial stage of the high speed impact, a thin liquid sheet (lamella) is rapidly ejected near a solid surface because the droplet is significantly compressed due to the strong inertial effect [29,68]. While the capillary effect still acts near the leading edge of the jetted lamella, the capillary wave cannot be propagated to the central part of the droplet since its propagation velocity is less than the impact speed [68]. Hence, the capillary waves are locked near the leading edge, forming a thick rounded rim (blob) [29,68]. The typical shape of spreading droplets for high speed impact cases can be characterized by a radially expanding lamella sheet bounded by a thick rim [29], and a quite different energy loss mechanism has been found (e.g., dissipation in the bulk, lamella, rim, shear boundary layer, and the residual vortical fluid motion, etc) [19,30,46]. Note that the regime transition from the low speed impact (capillary-driven spreading at low We) to the high speed impact (inertia-driven spreading at high We) has been observed on the order of We ~ 10 - 40 [29-31,69].

Finally, we observed similar dissipation trends to Figs.10-11 from the cases where We = 0 as well (i.e., spontaneous spreading cases without initial kinetic energy). Although a separate quantification of two energy loss quantities ($E_{d,o}$ and $E_{d,i}$) is difficult since the approximation of the time-dependent boundary layer thickness based on Re cannot be applicable due to the zero impact velocity (Re = 0), evident effects of the capillary waves on the spreading dynamics and the two observed energy dissipation mechanisms (i.e., the capillary-wave-induced dissipation and the near-wall dissipation) were found to be qualitatively similar with those shown in the present study.

IV. CONCLUSIONS

In this study, the energetic analysis and the energy loss mechanisms of a spreading droplet in the low Weber number regime are investigated. With detailed direct numerical simulation, the changes in the energy budget and the flow structures are captured in detail. It is shown that the spreading behavior at low Weber number is primarily dominated by the surface wettability and the associated capillary effects.

The energetic analysis presented in this study shows that on the hydrophilic surface, the real potential energy source driving the spreading process is the initial surface energy (which is transformed into kinetic energy as well as viscous dissipation), not the initial kinetic energy. This allows us to note the limitation of the conventional energy-balance-based approaches based on the assumption that the spreading is driven by the initial kinetic energy which is converted into surface energy and viscous dissipation during the spreading process. Such a conventional approach has been found to be valid only for the hydrophobic surface.

Particular attention is also paid to the role of the capillary waves. Most of the important flow physics, i.e., the (staircase-like) interfacial structure, the oscillatory motion of the central part of the liquid film and its collapse, the onset of the viscous regime, and the energy dissipation, are significantly affected by the capillary-wave-induced phenomena. It is also shown that the capillary-wave-induced energy dissipation can be estimated to be about 25-35% and about 55-65% of the total energy loss for the hydrophilic and the hydrophobic surface, respectively, and that such trends hold globally for a range of $1 \leq We \leq 10$, i.e., the capillary-driven spreading regime.

ACKNOWLEDGMENTS

This work was supported by the National Research Foundation of Korea (NRF) grants funded by the Korean government (MSIT) (2020R1A2C1003822) and support through computing time at the Institut du Developpement et des Ressources en Informatique Scientifique (IDRIS) of the Centre National de la Recherche Scientifique (CNRS), coordinated by GENCI (Grand Equipement National de Calcul Intensif) Grant 2022 A0122B06721.

DATA AVAILABILITY STATEMENTS

Data sharing is not applicable to this article because no new data were created or analyzed in this study.

FIGURES

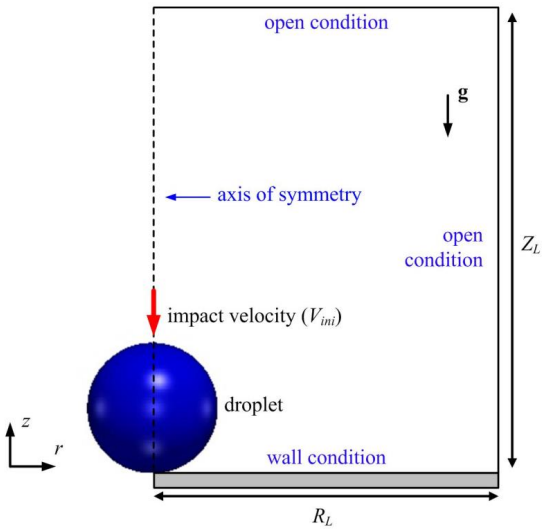

Fig. 1. Computational geometry and boundary conditions for the droplet impact on a solid surface.

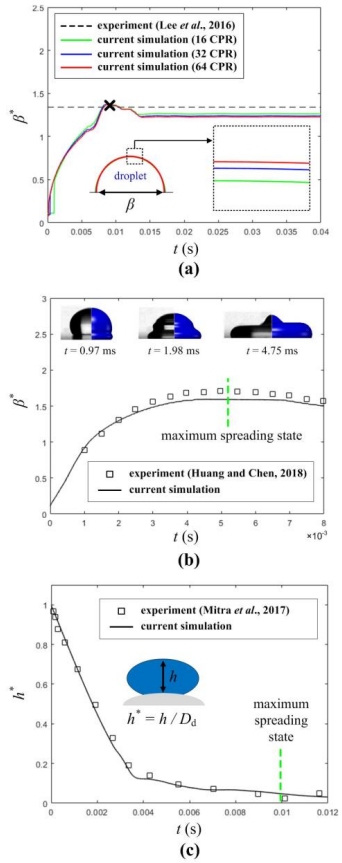

Fig. 2. Benchmark tests. (a) Evolution of the nondimensional spreading diameters ($\beta^*= \beta/D_d$) for a droplet spreading on a hydrophilic surface (steel, θ_{eqi} = 61°) at zero impact velocity (We = 0). The experimental result of Lee *et al*. [43] for the maximum value of β^* is marked by a black cross. The inset depicts the droplet morphologies simulated by using three different grid resolutions (16, 32, and 64 CPR) at t = 0.02 s. (b) Evolution of the nondimensional spreading diameter (β^*) for a droplet spreading on a hydrophobic surface (parafilm, θ_{eqi} = 110°) at low Weber number regime (We = 8.9). The experimental result of Huang and Chen [31] is marked by black squares. The insets compare the interfacial morphologies of the droplet between the experiment [31] and the current simulation for three different time instants (t = 0.97, 1.98, and 4.75 ms). Reproduced with permission from H. Huang and X. Chen, "Energetic analysis of drop's maximum spreading on solid surface with low impact speed", Phys. Fluids **30**, 022106 (2018). Copyright 2018 AIP Publishing LLC. (c) Evolution of the nondimensional film thickness ($h^*=h/D_d$) measured at the collision center for a droplet spreading on a neutral particle surface (brass, θ_{eqi} = 86°) at an intermediate Weber number regime (We = 19.1). The experimental result of Mitra *et al*. [60] is marked by black squares. The inset depicts the schematic diagram for measuring h^*.

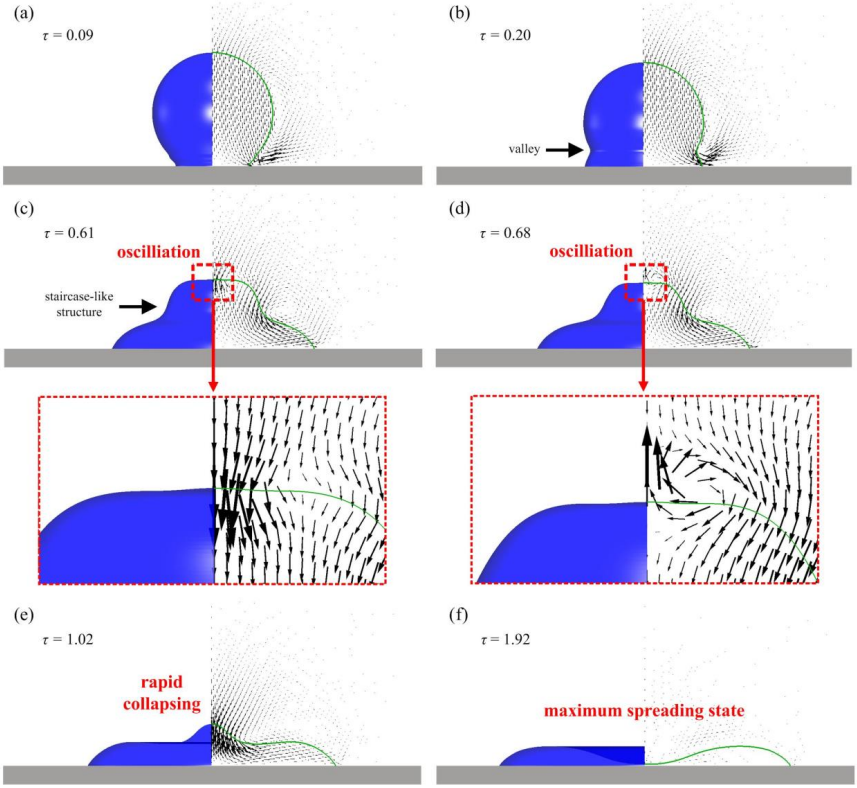

Fig. 3. Evolution of droplet morphologies (left image in each panel) and velocity vectors (right image in each panel) for the hydrophilic surface case. We = 3.5 and $\theta_{eqi} = 20°$. (a) $\tau = 0.09$, (b) $\tau = 0.20$, (c) $\tau = 0.61$, (d) $\tau = 0.68$, (e) $\tau = 1.02$, and (f) $\tau = 1.92$.

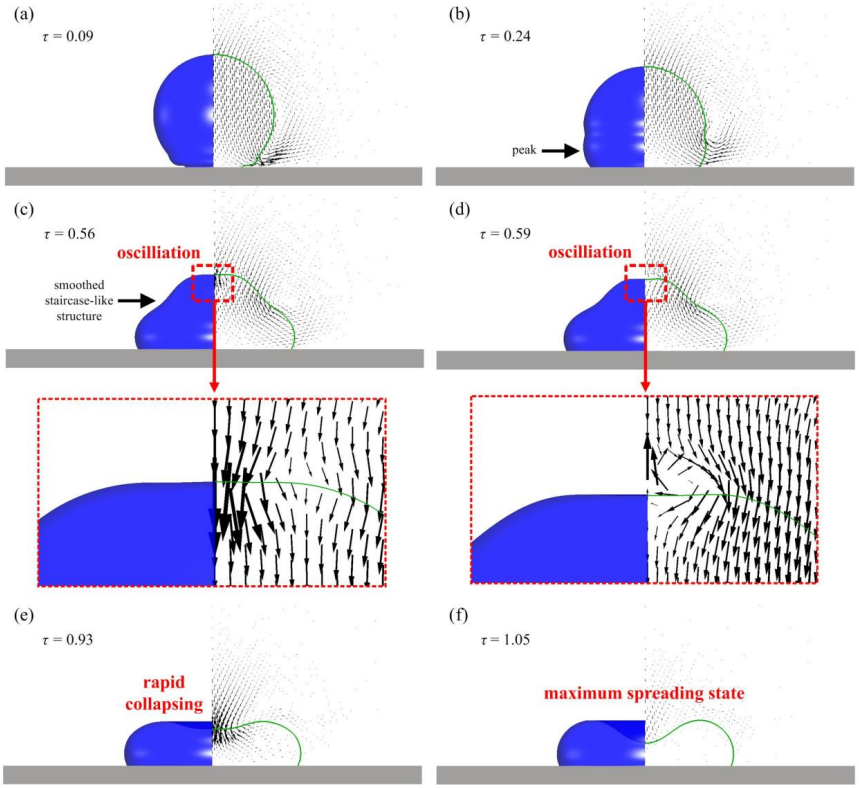

Fig. 4. Evolution of droplet morphologies (left image in each panel) and velocity vectors (right image in each panel) for the hydrophobic surface case. We = 3.5 and θ_{eqi} = 125°. (a) τ = 0.09, (b) τ = 0.24, (c) τ = 0.56, (d) τ = 0.59, (e) τ = 0.93, and (f) τ = 1.05.

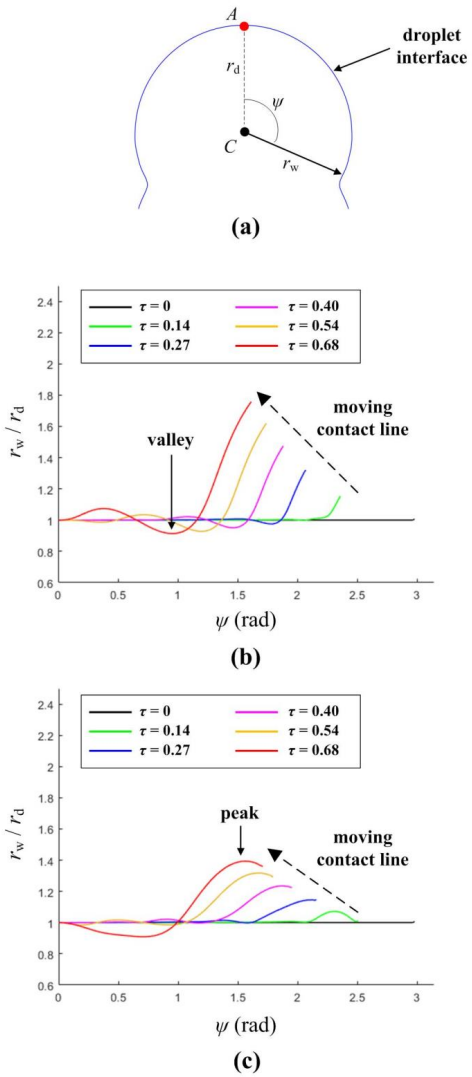

Fig. 5. Typical propagations of the capillary waves. (a) Schematic diagram for measuring r_w/r_d. (b) Wave propagation during droplet spreading on the hydrophilic surface (We = 3.5 and θ_{eqi} = 20°). (c) Wave propagation during droplet spreading on the hydrophobic surface (We = 3.5 and θ_{eqi} = 125°).

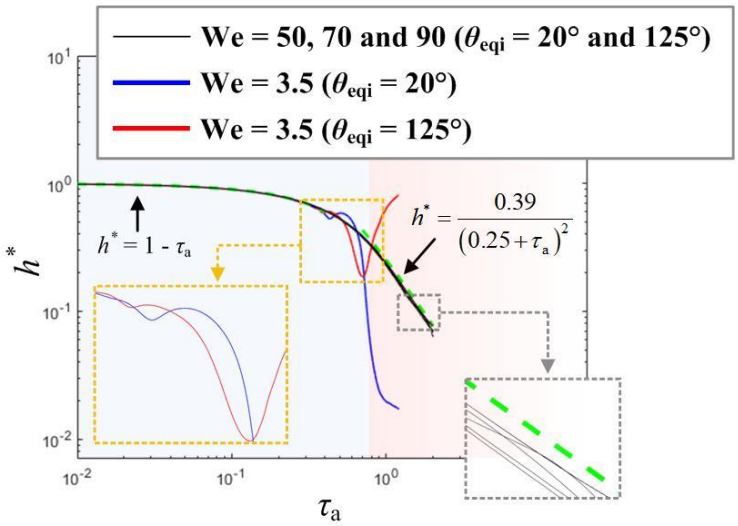

Fig. 6. Temporal variations of the nondimensional film thickness h^*. Two green dashed lines indicate the universal profiles of h^* for collision cases at the high Weber number regime: $h^* = 1 - \tau_a$ for the first (initial drop deformation) phase and $h^* = 0.39/(0.25+\tau_a)^2$ for the second (inertia dominated) phase [61]. Two different background colors also represent the first and the second phases of the universal profiles for the high Weber number regime.

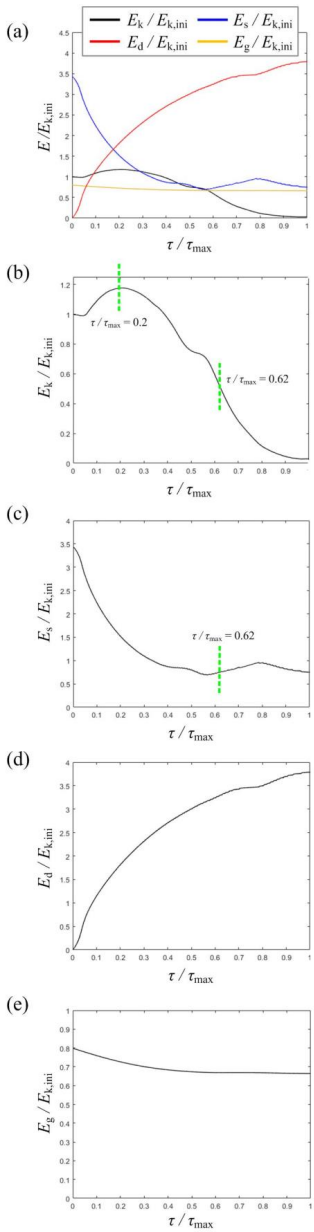

Fig. 7. Energetic analysis of the droplet collision for the hydrophilic surface case. We = 3.5 and θ_{eqi} = 20°. (a) changes in all energy components, (b) change in the kinetic energy, (c) change in the surface energy, (d) change in the viscous dissipation, and (e) change in the gravitational energy. All energy terms are normalized by the initial kinetic energy $E_{k,ini}$.

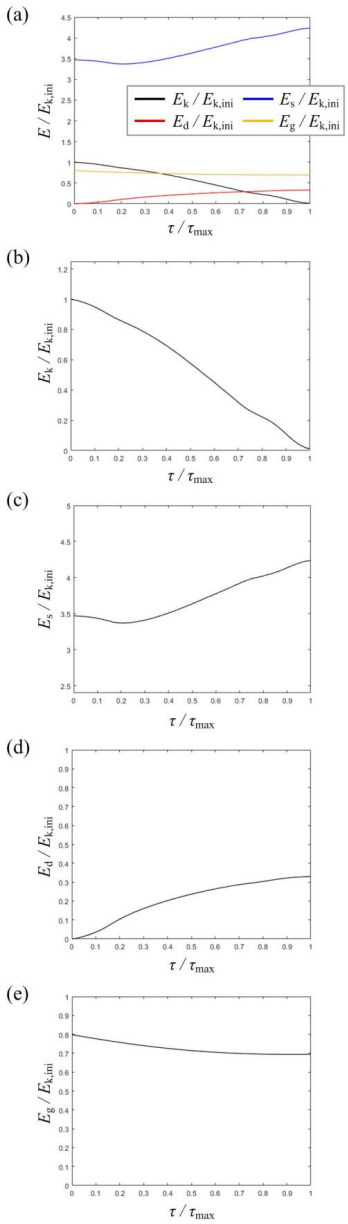

Fig. 8. Energetic analysis of the droplet collision for the hydrophobic surface case. We = 3.5 and θ_{eqi} = 125°. (a) changes in all energy components, (b) change in the kinetic energy, (c) change in the surface energy, (d) change in the viscous dissipation, and (e) change in the gravitational energy. All energy terms are normalized by the initial kinetic energy $E_{k,ini}$.

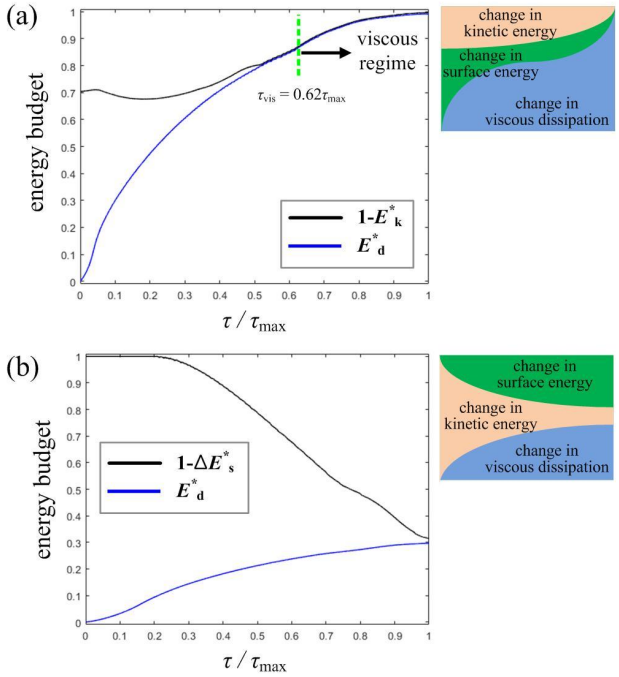

Fig. 9. Temporal changes in the energy budget. An example diagram is inserted to the upper-right corner of each subfigure, to clarify its physical interpretation. (a) Energy budget of the spreading droplet on the hydrophilic surface (We = 3.5 and $\theta_{eqi} = 20°$). E_k and E_d are normalized by ΔE_t, i.e., the total decrease in three energy sources ($\Delta E_t = \Delta E_k + \Delta E_s + \Delta E_g$). (b) Energy budget of the spreading droplet on the hydrophobic surface (We = 3.5 and $\theta_{eqi} = 125°$). ΔE_s and E_d are normalized by the initial kinetic energy $E_{k,ini}$.

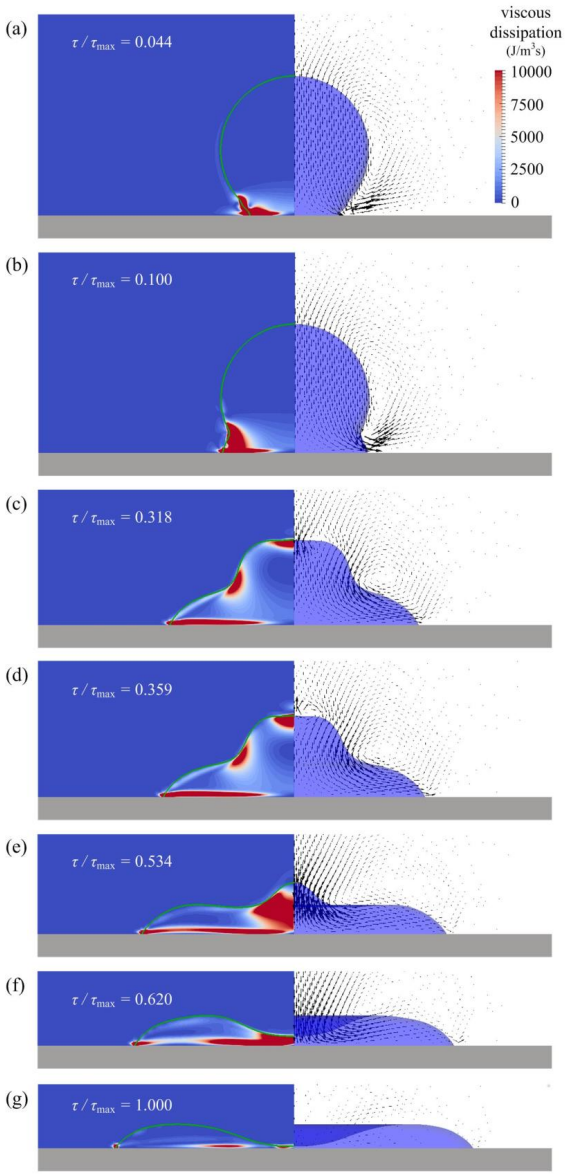

Fig. 10. Evolution of the energy dissipation fields (left image in each panel) and velocity vectors (right image in each panel) for the hydrophilic surface case. We = 3.5 and $\theta_{eqi} = 20°$. (a) $\tau / \tau_{max} = 0.044$, (b) $\tau / \tau_{max} = 0.100$, (c) $\tau / \tau_{max} = 0.318$, (d) $\tau / \tau_{max} = 0.359$, (e) $\tau / \tau_{max} = 0.534$, (f) $\tau / \tau_{max} = 0.620$ (i.e., τ_{vis}), and (g) $\tau / \tau_{max} = 1.000$.

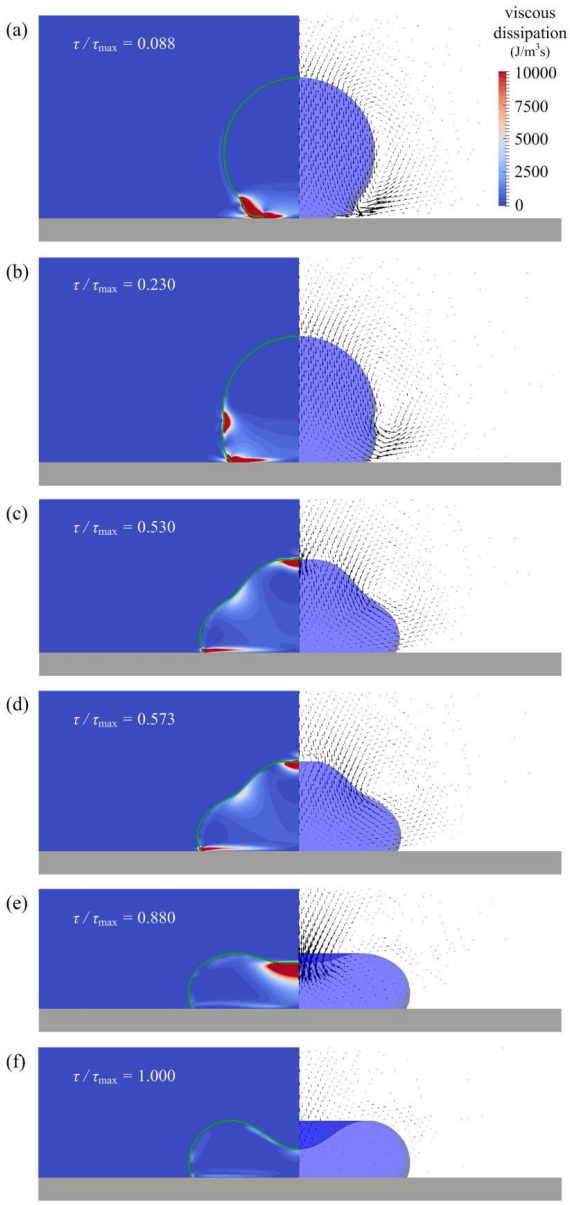

Fig. 11. Evolution of energy dissipation fields (left image in each panel) and velocity vectors (right image in each panel) for the hydrophobic surface case. We = 3.5 and $\theta_{eqi} = 125°$. (a) $\tau / \tau_{max} = 0.088$, (b) $\tau / \tau_{max} = 0.230$, (c) $\tau / \tau_{max} = 0.530$, (d) $\tau / \tau_{max} = 0.573$, (e) $\tau / \tau_{max} = 0.880$, and (f) $\tau / \tau_{max} = 1.000$.

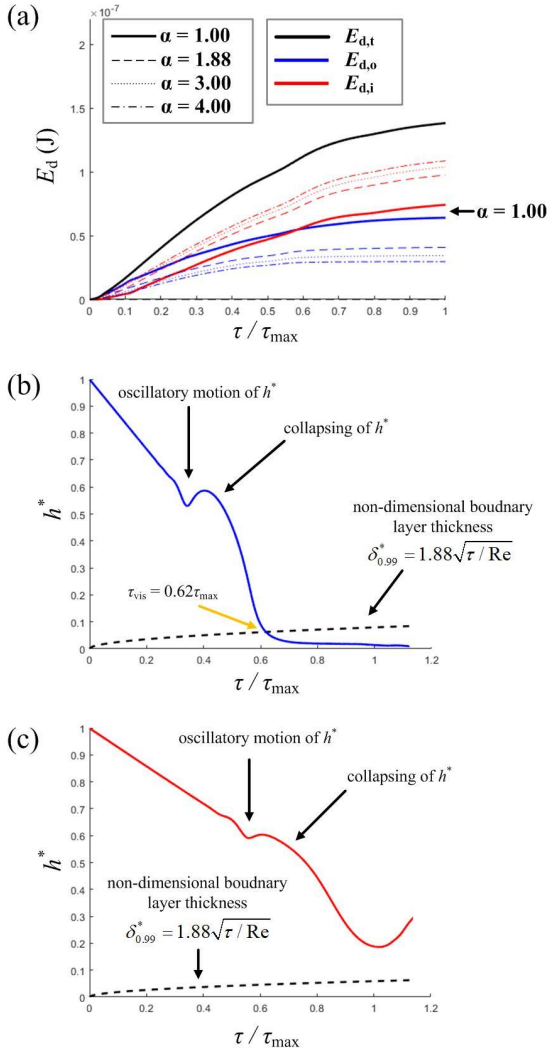

Fig. 12. (a) A preliminary test for the separate quantification of two energy dissipation quantities (the capillary-wave-induced dissipation in the outer flow region and the near wall dissipation in the boundary layer) for 4 different numerical prefactors (α = 1.00, 1.88, 3.00, and 4.00). The collision case shown in Figs. 3,7, and 10 are chosen for the test. (b) Temporal variations of the nondimensional film thickness h^* and nondimensional boundary layer thickness $\delta^*_{0.99}$ for the hydrophilic surface (We = 3.5 and θ_{eqi} = 20°). (c) Temporal variations of the nondimensional film thickness h^* and nondimensional boundary layer thickness $\delta^*_{0.99}$ for the hydrophobic surface (We = 3.5 and θ_{eqi} = 125°).

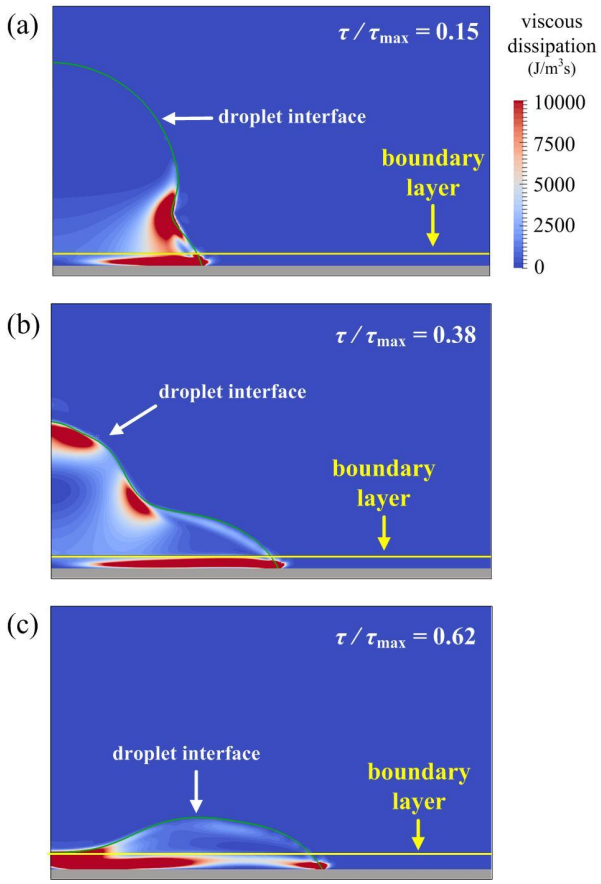

Fig. 13. Evolution of the energy dissipation fields (We = 3.5 and θ_{eqi} = 20°). The time-dependent growing boundary layers are plotted together. (a) τ / τ_{max} = 0.15, (b) τ / τ_{max} = 0.38, and (c) τ / τ_{max} = 0.62 (i.e., τ_{vis}).

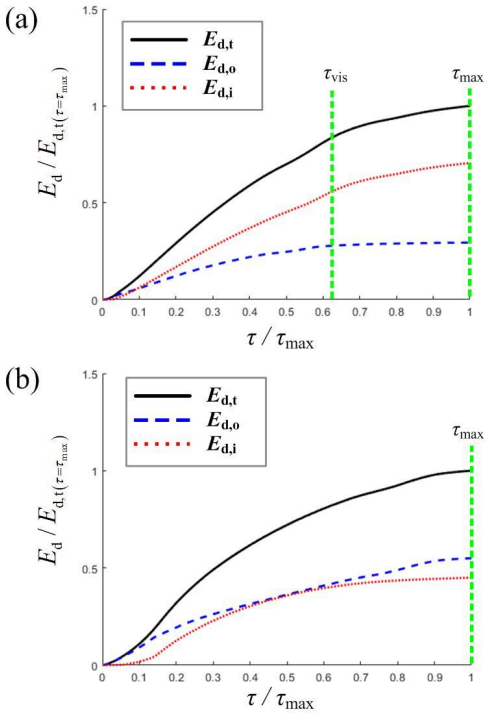

Fig. 14. Comparisons of two energy dissipation quantities: the capillary-wave-induced dissipation ($E_{d,o}$) and the near wall dissipation ($E_{d,i}$). We = 3.5. (a) hydrophilic surface (θ_{eqi} = 20°), and (b) hydrophobic surface (θ_{eqi} = 125°).

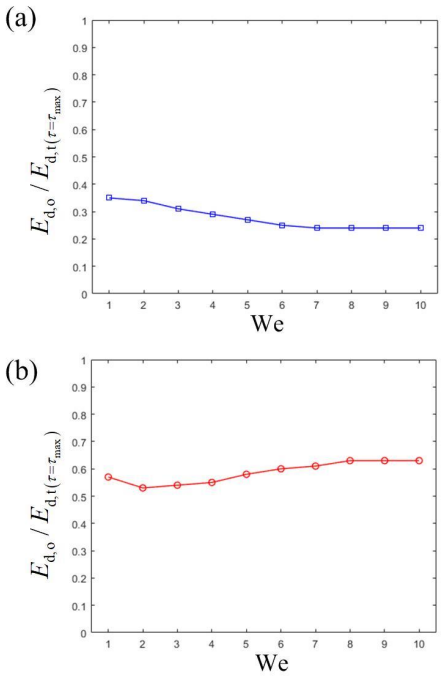

Fig. 15. Share of the capillary-wave-induced dissipation ($E_{d,o}$) to the total energy dissipation ($E_{d,t}$) as a function of Weber number. (a) hydrophilic surface (θ_{eqi} = 20°), and (b) hydrophobic surface (θ_{eqi} = 125°).

References

1. D. Lohse, "Fundamental fluid dynamics challenges in inkjet printing," Annu. Rev. Fluid Mech. **54**, 349–382 (2021).

2. R. Daly, T. S. Harrington, G. D. Martin, and I. M. Hutchings, "Inkjet printing for pharmaceutics—A review of research and manufacturing," Int. J. Pharm. **494** (2), 554–567 (2015).

3. N. Lann, K. G. Bruin, D. Slenter, J. Wilhelm, M. Jermy, and D. Bonn, "Bloodstain pattern analysis: Implementation of a fluid dynamic model for position determination of victims," Sci. Rep. **5**, 11461 (2015).

4. S. Yun, "Controlling the rebound on a solid surface by varying impact angles of ellipsoidal drops," Phys. Fluids **33**, 042105 (2021).

5. A. Marmur, "The lotus effect: Superhydrophobicity and metastability," Langmuir **20** (9), 3517–3519 (2004).

6. G. Charalampous and Y. Hardalupas, "Collisions of droplets on spherical particles," Phys. Fluids **29**, 103305 (2017).

7. J. D. Oxley, "5 - Spray cooling and spray chilling for food ingredient and nutraceutical encapsulation," Encapsulation Technologies and Delivery Systems for Food Ingredients and Nutraceuticals, Woodhead Publishing, 110-130 (2012).

8. E. Teunou, and D. Poncelet, "Batch and continuous fluid bed coating – review and state of the art," Journal of Food Engineering, **53** (4), 325-340 (2002).

9. A. Kundu, K. D. P. Nigam and R. P. Verma, "Catalyst wetting characteristics in trickle-bed reactors," AIChE J. **49** (9), 2253-2263 (2003).

10. D. Khojasteh, N. M. Kazerooni, and M. Marengo, "A review of liquid droplet impacting onto solid spherical particles: A physical pathway to encapsulation mechanisms," J. Ind. Eng. Chem. **71**, 50–64 (2019).

11. A. L. Yarin, "Drop Impact Dynamics: Splashing, Spreading, Receding, Bouncing, ...," Annu. Rev. Fluid Mech. **38**, 159 (2006).

12. C. Josserand and S. T. Thoroddsen, "Drop impact on a solid surface," Annu. Rev. Fluid Mech. **48**, 365–391 (2016).

13. M. Marengo, C. Antonini, I. V. Roisman, and C. Tropea, "Drop collisions with simple and complex surfaces," Curr. Opin. Colloid Interface Sci. **16** (4), 292–302 (2011).

14. W. Fang, K. Zhang, Q. Jiang, C. Lv, C. Sun, Q. Li, Y. Song, and X. Feng, "Drop impact dynamics on solid surfaces", Appl. Phys. Lett. **121**, 210501 (2022).

15. A. Mongruel, V. Daru, F. Feuillebois, and S. Tabakova , "Early post-impact time dynamics of viscous drops onto a solid dry surface", Phys. Fluids **21**, 032101 (2009).

16. Š. Šikalo, H.-D. Wilhelm, I. V. Roisman, S. Jakirlić, and C. Tropea, "Dynamic contact angle of spreading droplets: Experiments and simulations," Phys. Fluids **17**, 062103 (2005).

17. C. Antonini, A. Amirfazli, and M. Marengo, "Drop impact and wettability: From hydrophilic to superhydrophobic surfaces," Phys. Fluids **24**, 102104 (2012).

18. H. Almohammadi and A. Amirfazli, "Droplet impact: Viscosity and wettability effects on splashing," Journal of Colloid and Interface Science **553**, 22-30 (2019).

19. C. Clanet, C. Béguin, D. Richard, and D. Quéré, "Maximal deformation of an impacting drop," J. Fluid Mech. **517**, 199–208 (2004).

20. D. Bartolo, C. Josserand, and D. Bonn, "Retraction dynamics of aqueous drops upon impact on non-wetting surfaces", J. Fluid Mech. **545**, 329–338 (2005).

21. B. Derby, "Inkjet printing of functional and structural materials: Fluid property requirements, feature stability and resolution," Annu. Rev. Mater. Res. 40, 395 (2010).

22. F. Gao and A. A. Sonin, "Precise deposition of molten microdrops: the physics of digital microfabrication," Proc. R. Soc. Lond. A **444**, 533–554 (1994).

23. I. Yoon, J. Chergui, D. Juric, and S. Shin, "Maximum spreading of droplet-particle collision covering a low Weber number regime and data-driven prediction model," Phys. Fluids **34**, 102109 (2022).

24. S. Chandra and C. T. Avedisian, "On the collision of a droplet with a solid surface," Proc. R. Soc. London A **432**, 13 (1991).

25. M. Pasandideh-Fard, Y. Qiao, S. Chandra, and J. Mostaghimi, "Capillary effects during droplet impact on a solid surface," Phys. Fluids **8**, 650 (1996).

26. T. Mao, D. Kuhn, and H. Tran, "Spread and rebound of liquid droplets upon impact on flat surfaces," AIChE J. **43**, 2169–2179 (1997).

27. C. Ukiwe and D. Y. Kwok, "On the maximum spreading diameter of impacting droplets on well-prepared solid surfaces," Langmuir **21**, 2, 666–673 (2005).

28. F. Wang, L. Yang, L. Wang, Y. Zhu, and T. Fang, "Maximum Spread of Droplet Impacting onto Solid Surfaces with Different Wettabilities: Adopting a Rim–Lamella Shape," Langmuir **35**, 3204-3214 (2019).

29. I. V. Roisman, "Inertia dominated drop collisions. II. An analytical solution of the Navier–Stokes's equations for a spreading viscous film," Phys. Fluids **21**, 052104 (2009).

30. S. Wildeman, C. Visser, C. Sun, and D. Lohse, "On the spreading of impacting drops," J. Fluid Mech. **805**, 636–655 (2016).

31. H. Huang and X. Chen, "Energetic analysis of drop's maximum spreading on solid surface with low impact speed", Phys. Fluids **30**, 022106 (2018).

32. J. B. Lee, D. Derome, R. Guyer, and J. Carmeliet, "Modeling the Maximum Spreading of Liquid Droplets Impacting Wetting and Nonwetting Surfaces," Langmuir **32**, 1299-1308 (2016).

33. S. Lin, B. Zhao, S. Zou, J. Guo, Z. Wei, and L. Chen, "Impact of viscous droplets on different wettable surfaces: Impact phenomena, the maximum spreading factor, spreading time and post-impact oscillation," Journal of Colloid and Interface Science, **516**, 86-97 (2018).

34. J. Du, X. Wang, Y. Li, Q. Min, and X. Wu, "Analytical Consideration for the Maximum Spreading Factor of Liquid Droplet Impact on a Smooth Solid Surface," Langmuir 37, 7582-7590 (2021).

35. Y. T. Aksoy, P. Eneren, E. Koos, and M. R. Vetrano, "Spreading of a droplet impacting on a smooth flat surface: How liquid viscosity influences the maximum spreading time and spreading ratio," Phys. Fluids. **34**, 042106 (2022).

36. Y. Xu, S. Vincent, QC. He, H. Le-Quang, "Spreading Time of Liquid Droplets Impacting on Non-wetting Solid Surfaces," Turbulence and Interactions: Notes on Numerical Fluid Mechanics and Multidisciplinary Design **149**, Springer, Cham. (2021).

37. B. L. Scheller, and D. W. Bousfield, "Newtonian drop impact with a solid surface." AIChE J. **41**,1357–1367 (1995).

38. N. Laan, K. G. de Bruin, D. Bartolo, C. Josserand, and D. Bonn, "Maximum Diameter of Impacting Liquid Droplets,", Phys. Rev. Applied 2, 044018 (2014).

39. I. Yoon and S. Shin, "Maximal spreading of droplet during collision on particle: effects of liquid viscosity and surface curvature," Phys. Fluids **33**, 083310 (2021).

40. H. Park, , W. W. Carr, J. Zhu, and J. F. Morris, "Single drop impaction on a solid surface," AIChE J. **49**, 2461-2471 (2003).

41. J. Eggers, M. A. Fontelos, C. Josserand, and S. Zaleski, "Drop dynamics after impact on a solid wall: Theory and simulations," Phys. Fluids **22**, 062101 (2010).

42. I. V. Roisman, R. Rioboo, and C. Tropea, "Normal impact of a liquid drop on a dry surface: Model for spreading and receding," Proc. R. Soc. Lond. A. **458**, 1411–1430 (2002).

43. J. B. Lee, N. Laan, K. G. De Bruin, G. Skantzaris, N. Shahidzadeh, D. Derome, J. Carmeliet, and C. Bonn, "Universal rescaling of drop impact on smooth and rough surfaces," J. Fluid Mech. **786**, R4 (2016).

44. H. N. Dalgamoni and X. Yong, "Numerical and theoretical modeling of droplet impact on spherical surfaces," Phys. Fluids **33**, 052112 (2021).

45. P. K. Sharma and H. N. Dixit, "Energetics of a bouncing drop: Coefficient of restitution, bubble entrapment, and escape," Phys. Fluids **32**, 112107 (2020).

46. Y. Renardy, S. Popinet, L. Duchemin, M. Renardy, S. Zaleski, C. Josserand, … and D. Quéré, "Pyramidal and toroidal water drops after impact on a solid surface," J. Fluid Mech. **484**, 69-83 (2003).

47. I. Yoon, C. Ha, C. Lee, and S. Shin, "Promoting rebound from droplet impact on a spherical particle: Experimental and numerical study," Phys. Fluids **34**, 103302 (2022).

48. I. Yoon and S. Shin, "Direct numerical simulation of droplet collision with stationary spherical particle: A comprehensive map of outcomes," Int. J. Multiph. Flow **135**, 103503 (2021).

49. G. Tryggvason, B. Bunner, A. Esmaeeli, D. Juric, N. Al-Rawahi, W. Tauber, J. Han, S. Nas, and Y.-J. Jan, "A Front-Tracking Method for the Computations of Multiphase Flow," J. Comput. Phys. 169 (2), 708-759 (2001).

50. J. U. Brackbill, D. B. Kothe and C. Zemach, "A continuum method for modeling surface tension," J. Comput. Phys. 100 (2), 335-354 (1992).

51. S. Shin, and D. Juric, "Modeling three-dimensional multiphase flow using a level contour reconstruction method for front tracking without connectivity," J. Comput. Phys. **180**, 427–470 (2002).

52. S. Shin and D. Juric, "A hybrid interface method for three-dimensional multiphase flows based on front tracking and level set techniques," Int. J. Numer. Meth. Fluids **60,** 753–778 (2009).

53. S. Shin, J. Chergui, and D. Juric, "Direct simulation of multiphase flows with modeling of dynamic interface contact," Theor. Comput. Fluid Dyn. **32**, 655–687 (2018).

54. S. Unverdi, and G. Tryggvason, "A front-tracking method for viscous, incompressible, multi-fluid flows," J. Comput. Phys. **100**, 25–37 (1992).

55. S. Osher and J. Sethian, "Fronts propagating with curvature-dependent speed: Algorithms based on Hamilton-Jacobi formulations," J. Comput. Phys. **79**, 12–49 (1988).

56. K. Yokoi, D. Vadillo, J. Hinch, and I. Hutchings, "Numerical studies of the influence of the dynamic contact angle on a droplet impacting on a dry surface," Phys. Fluids **21**, 072102 (2009).

57. I. Yoon, J. Chergui, D. Juric, and S. Shin, "Adaptive mesh axi-symmetric simulation of droplet impact with a spherical particle in mid-air," Int. J. Multiph. Flow **155**, 104193 (2022).

58. G. Khurana, N. Sahoo, and P. Dhar, "Phenomenology of droplet collision hydrodynamics on wetting and non-wetting spheres," Phys. Fluids **31**, 072003 (2019).

59. P. Attané, F. Girard, v. Morin, "An energy balance approach of the dynamics of drop impact on a solid surface," Phys. Fluids **19**, 012101 (2007).

60. S. Mitra, G. M. Evans, E. Doroodchi, V. Pareek, and J. B. Joshi, "Interactions in droplet and particle system of near unity size ratio," Chem. Eng. Sci. 170, 154–175 (2017).

61. I. V. Roisman, E. Berberović, and C. Tropea, "Inertia dominated drop collisions. I. On the universal flow in the lamella," Phys. Fluids **21**, 052103 (2009).

62. S. Bakshi, I. V. Roisman, and C. Tropea, "Investigations on the impact of a drop onto a small spherical target," Phys. Fluids **19**, 032102 (2007).

63. H. Ding and P. Spelt, "Inertial effects in droplet spreading: A comparison between diffuse-interface and level-set simulations," J. Fluid Mech. **576**, 287-296 (2007).

64. J. Du, N. T. Chamakos, A. G. Papathanasiou, and Q. Min, "Initial spreading dynamics of a liquid droplet: The effects of wettability, liquid properties, and substrate topography," Phys. Fluids. **33**, 042118 (2021).

65. H. Ding, E. Li, F. Zhang, Y. Sui, P. Spelt, and S. Thoroddsen, "Propagation of capillary waves and ejection of small droplets in rapid droplet spreading," J. Fluid Mech. **697**, 92-114 (2012).

66. A. Yarin, and D. Weiss, "Impact of drops on solid surfaces: Self-similar capillary waves, and splashing as a new type of kinematic discontinuity," J. Fluid Mech. **283**, 141-173 (1995).

67. J. C. Bird, S. Mandre, and H. A. Stone, "Short-Time Dynamics of Partial Wetting," Phys. Rev. Lett. **100** (23), 234501 (2008).

68. A. I. Fedorchenko, and A. B. Wang, "The formation and dynamics of a blob on free and wall sheets induced by a drop impact on surfaces," Phys. Fluids **16**, 3911–3920 (2004).

69. S. Lin, Y. Wang, L. Sun, A. A. Mehrizi, Y. Jin, and L. Chen, "Experimental and numerical investigations on the spreading dynamics of impinging liquid droplets on diverse wettable surfaces," Int. J. Multiph. Flow **153**, 104135 (2022).

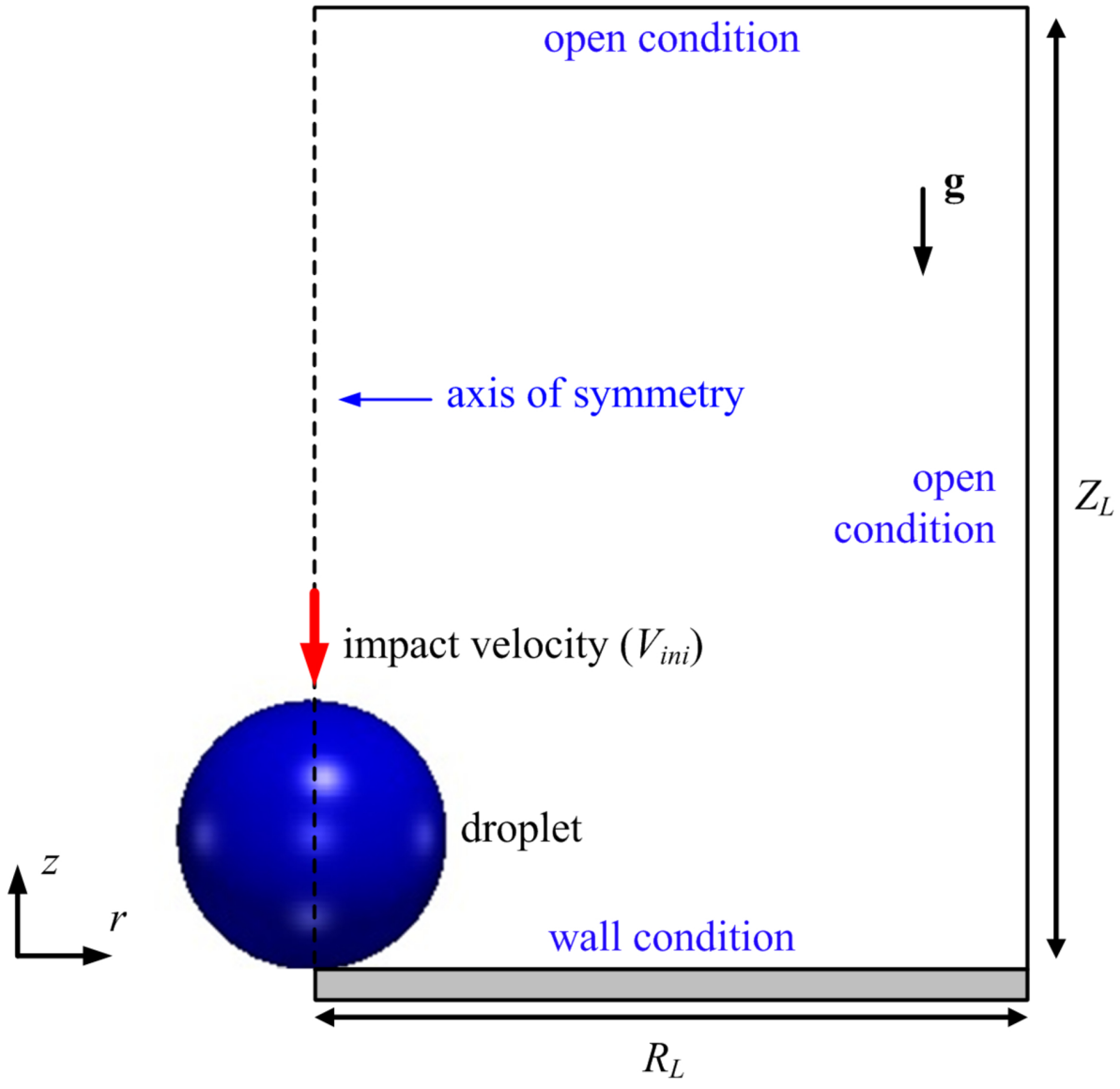

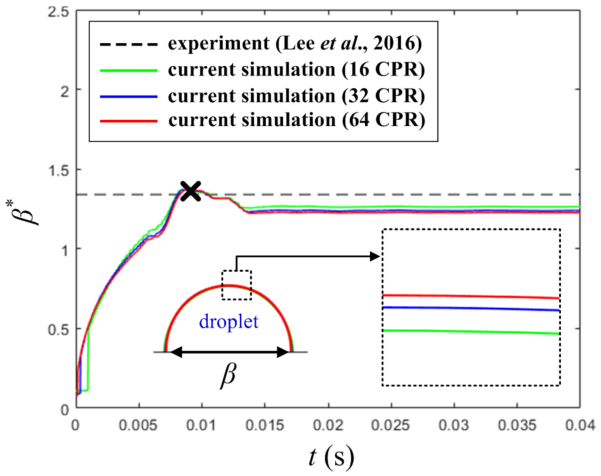

(a)

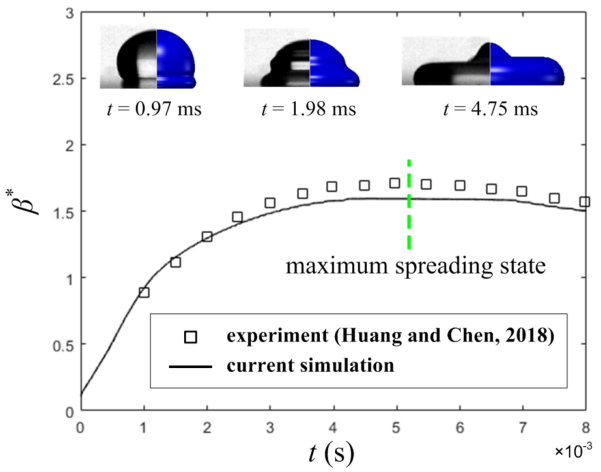

(b)

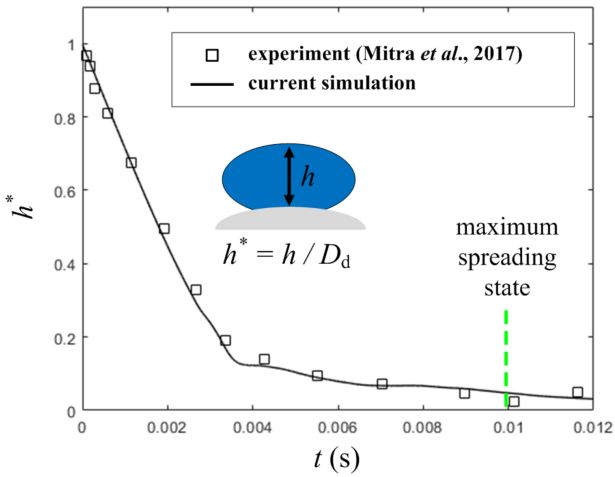

(c)

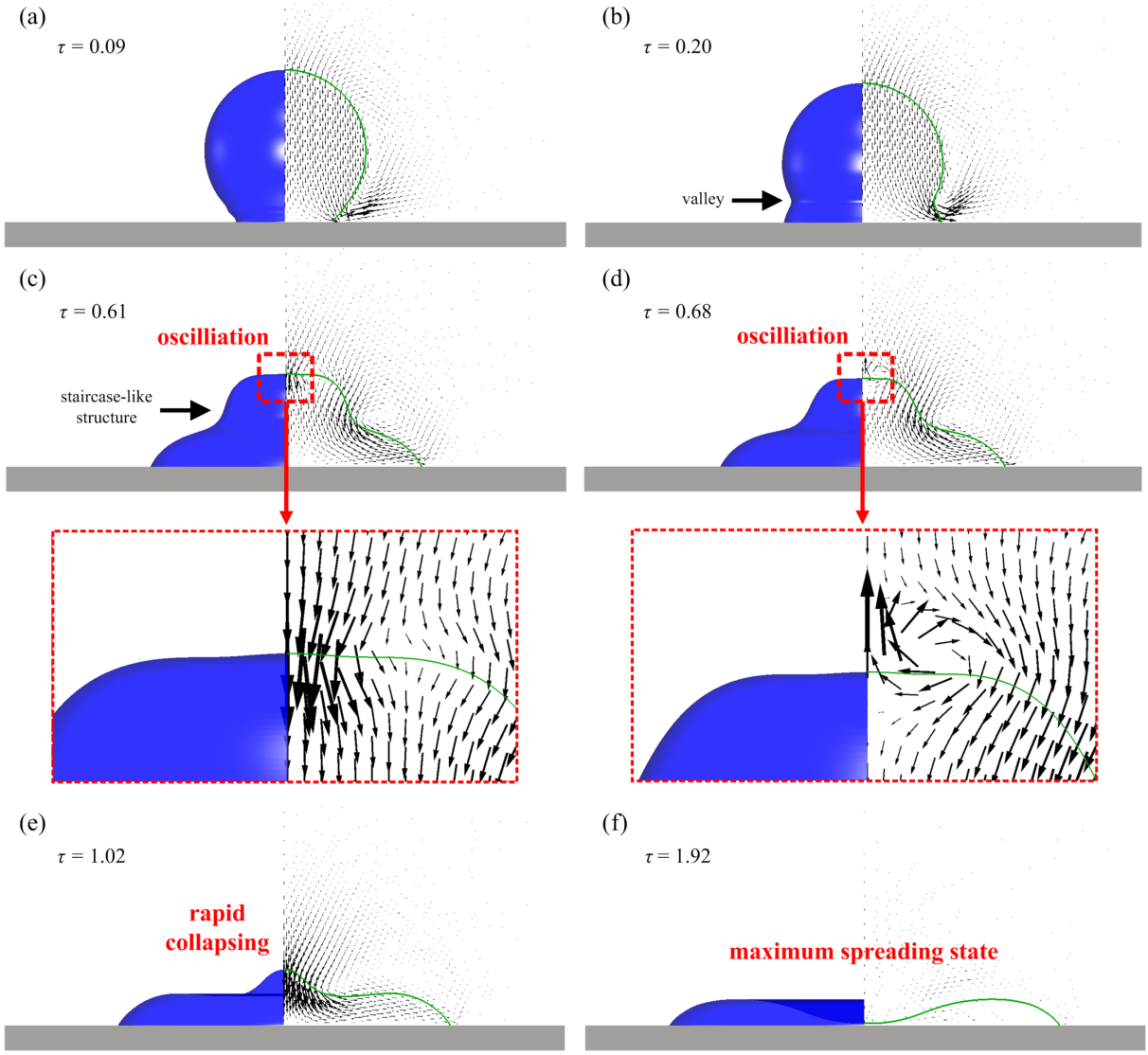

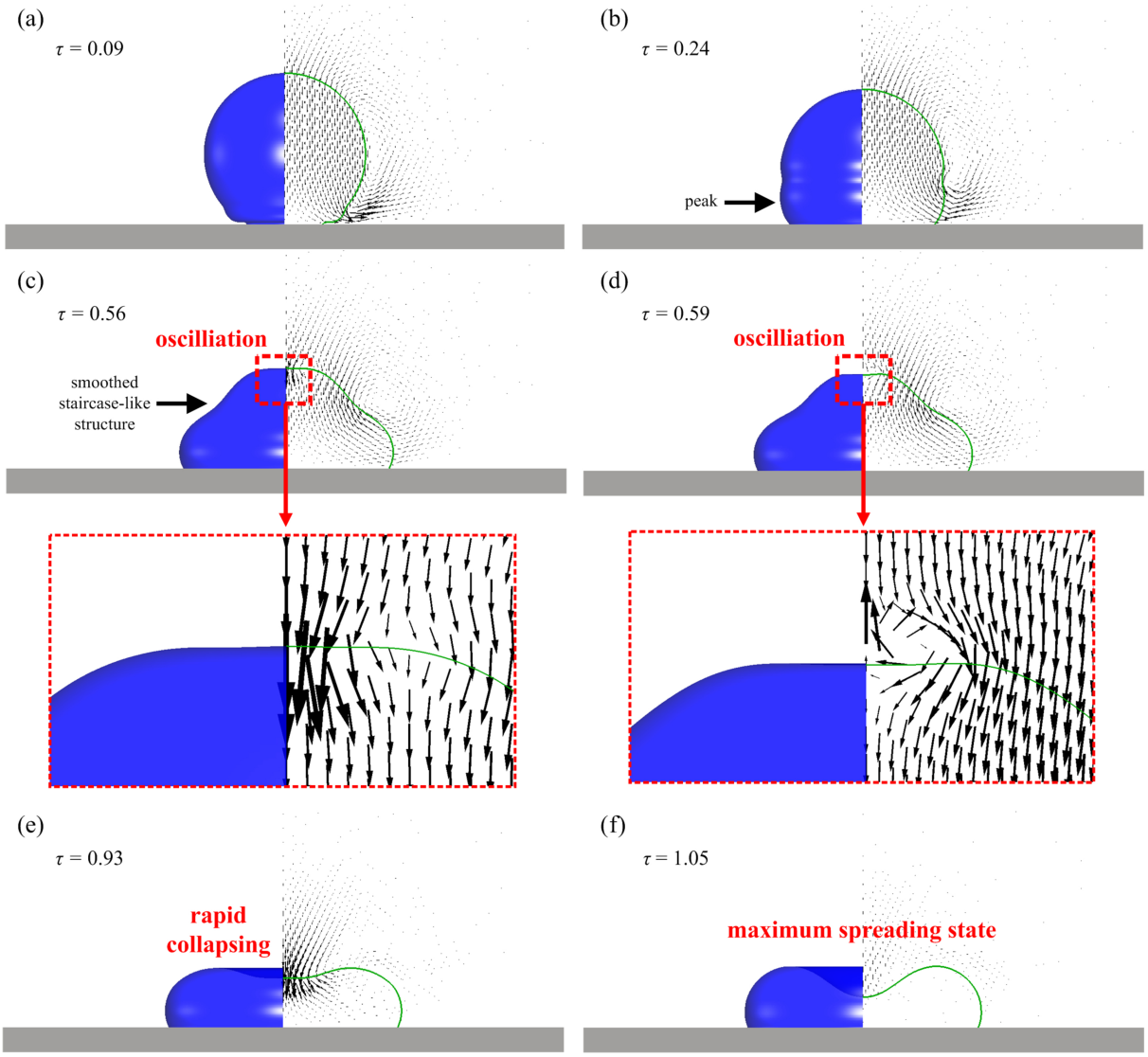

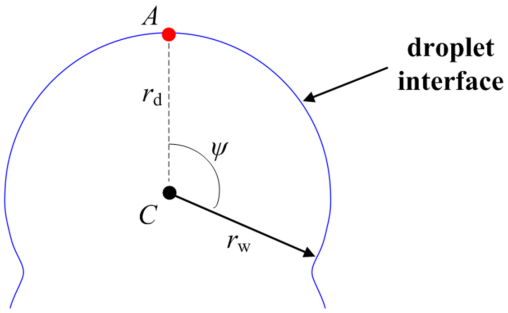

(a)

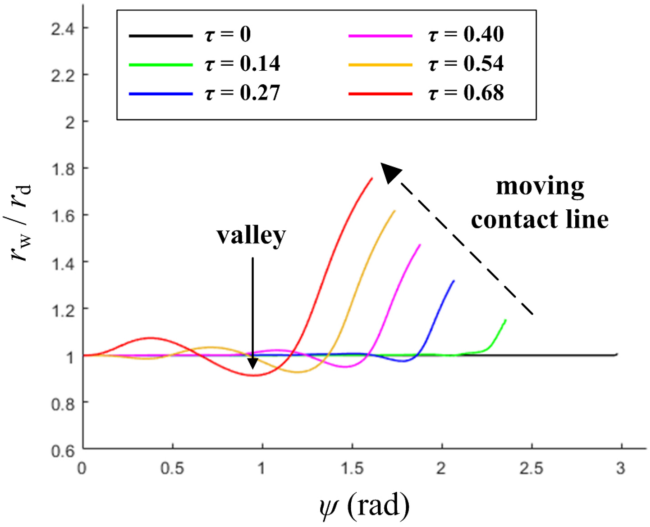

(b)

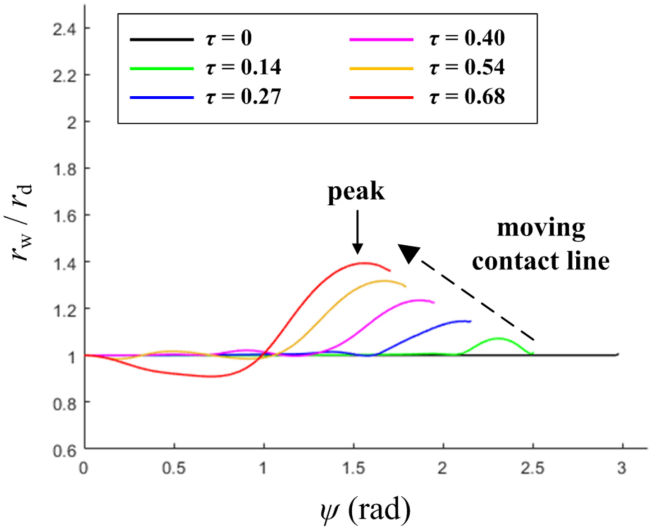

(c)

PLEASE CITE THIS ARTICLE AS DOI: 10.1063/5.0138378

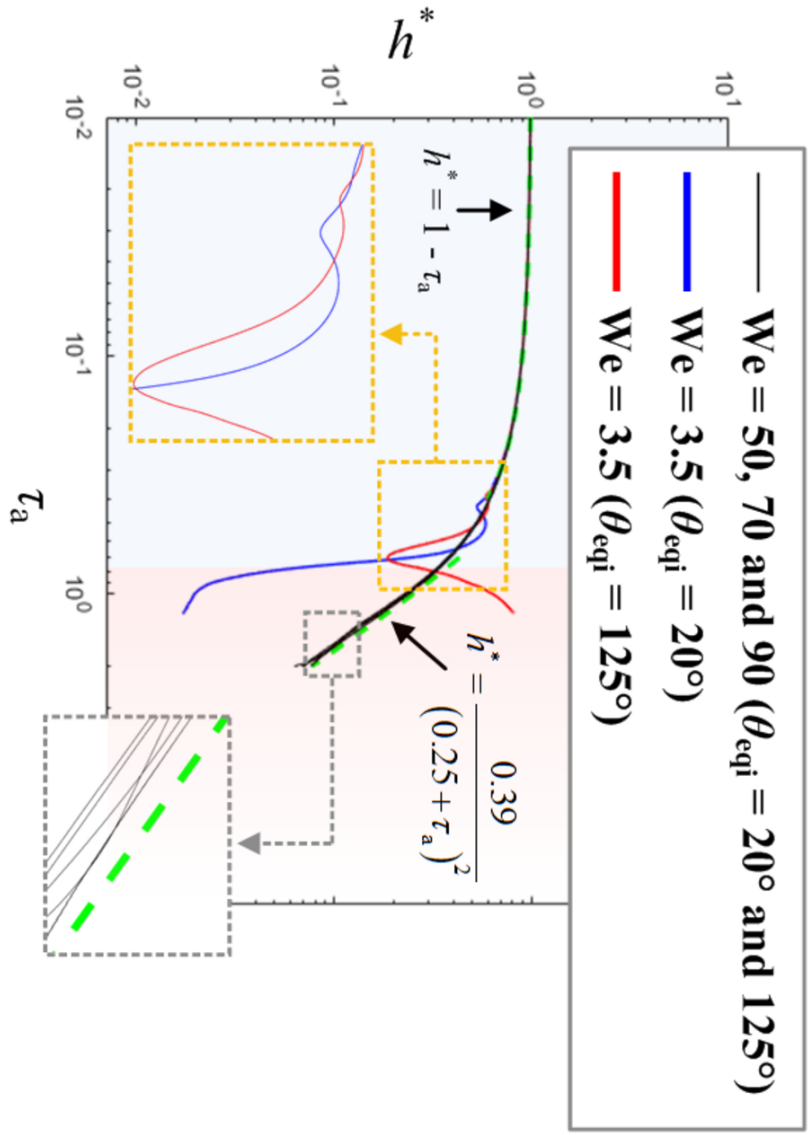

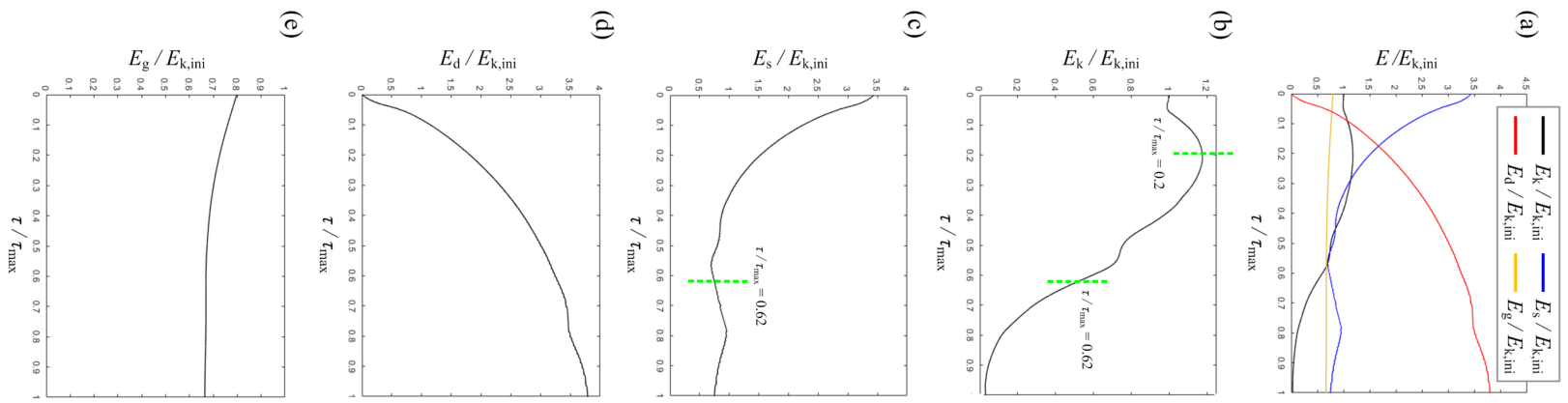

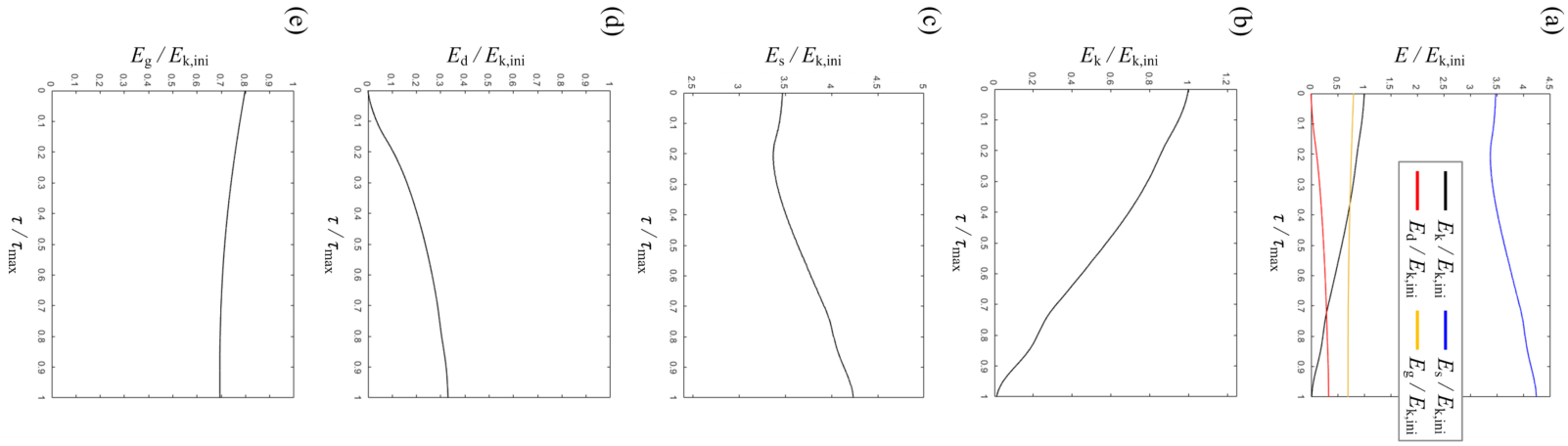

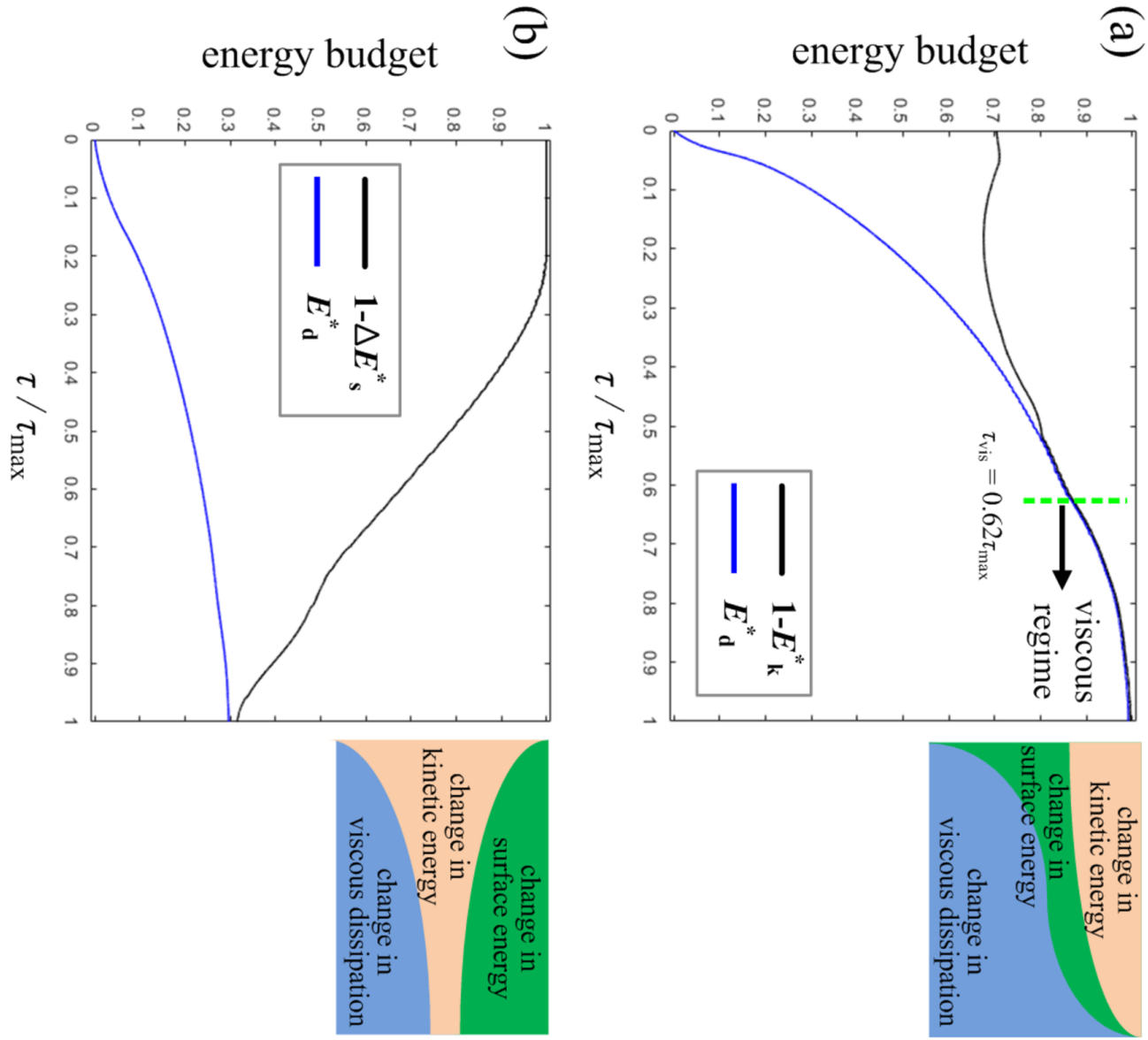

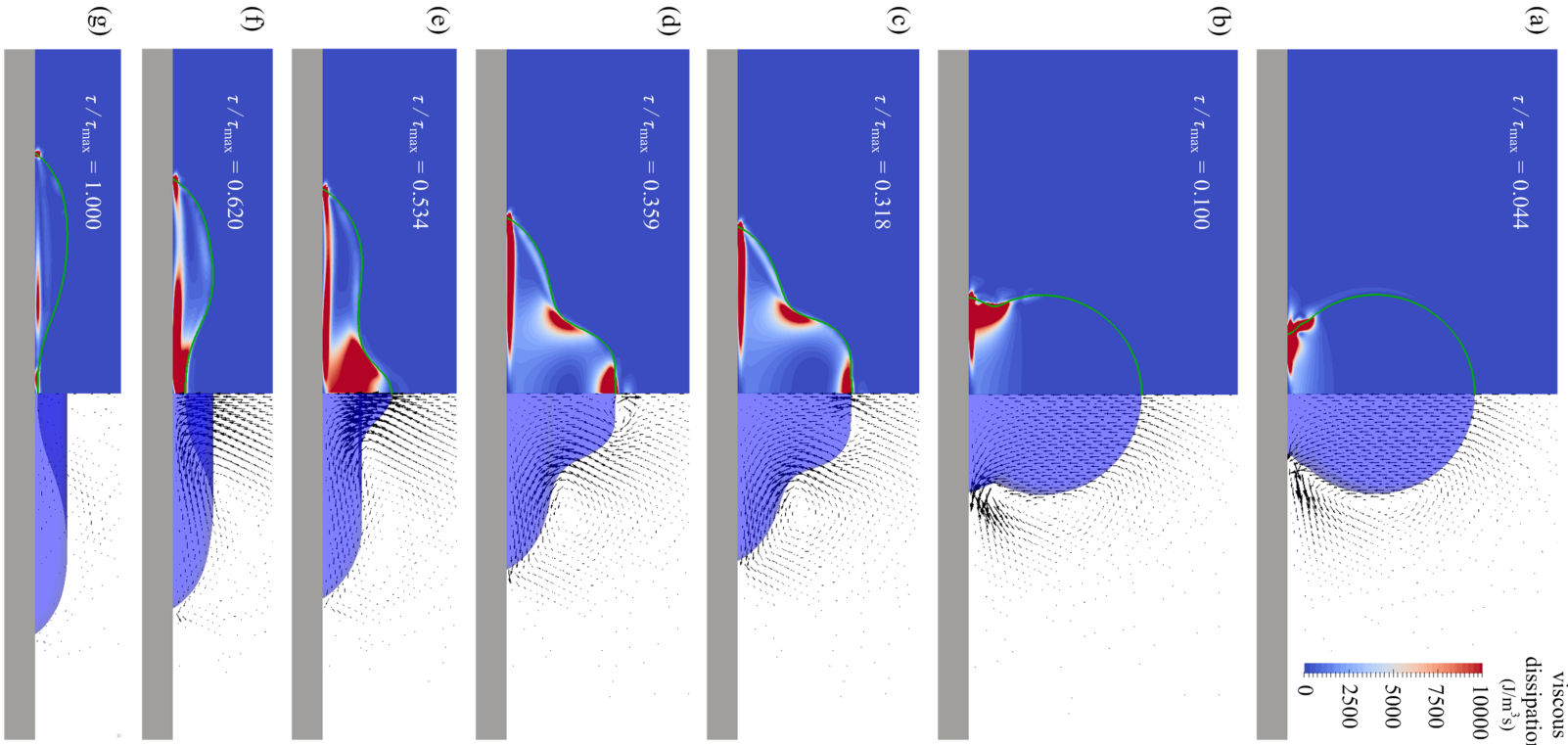

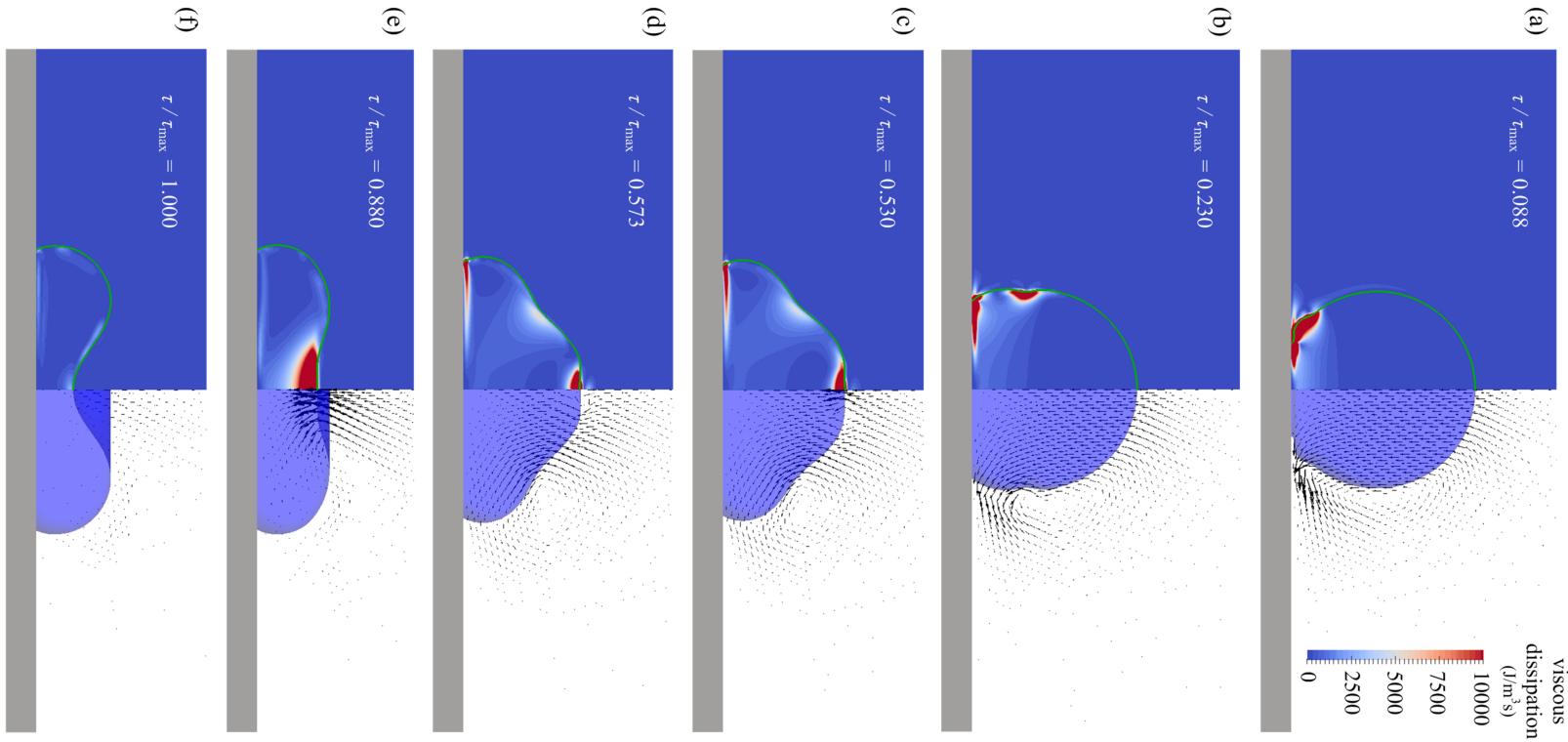

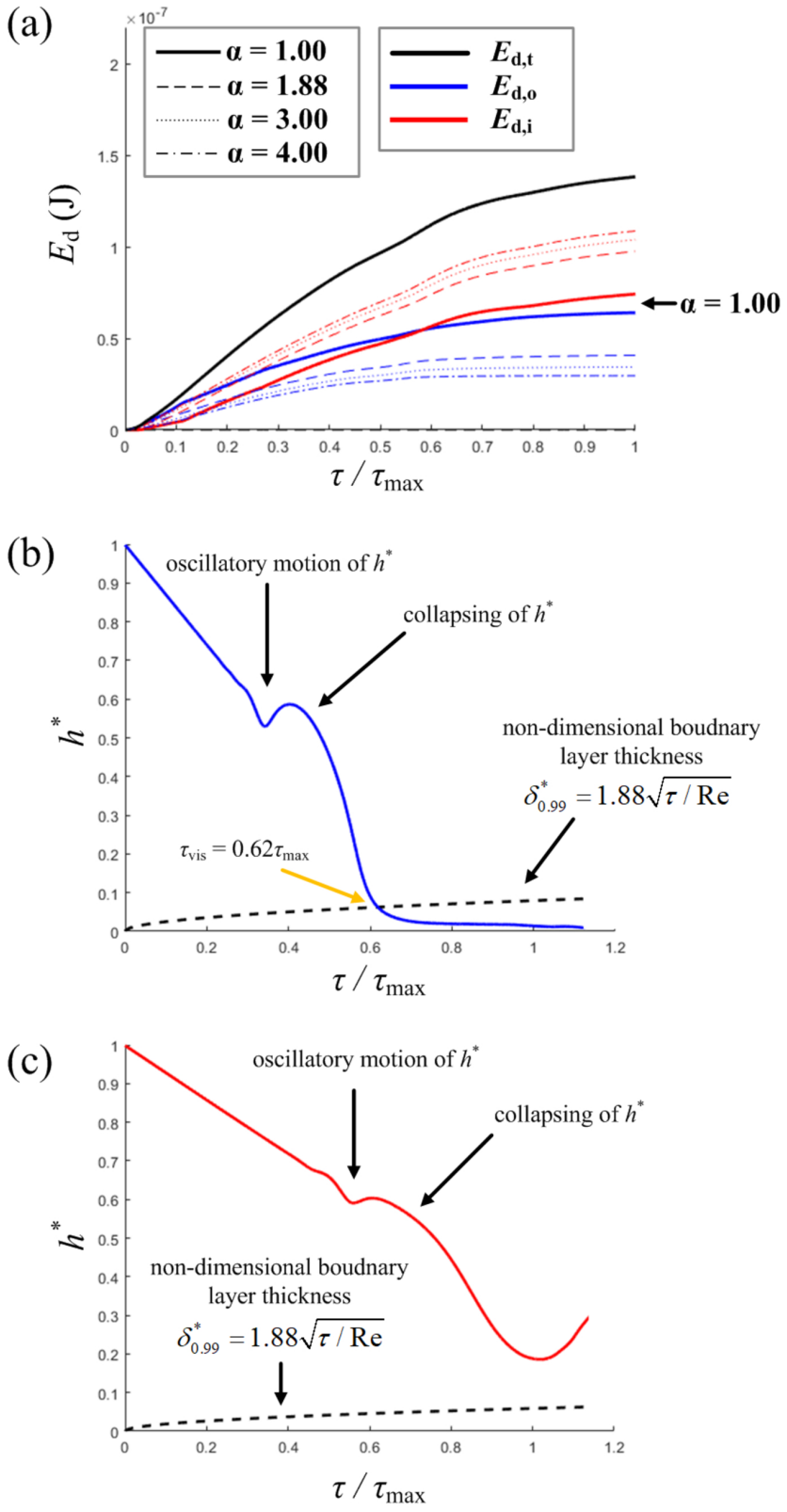

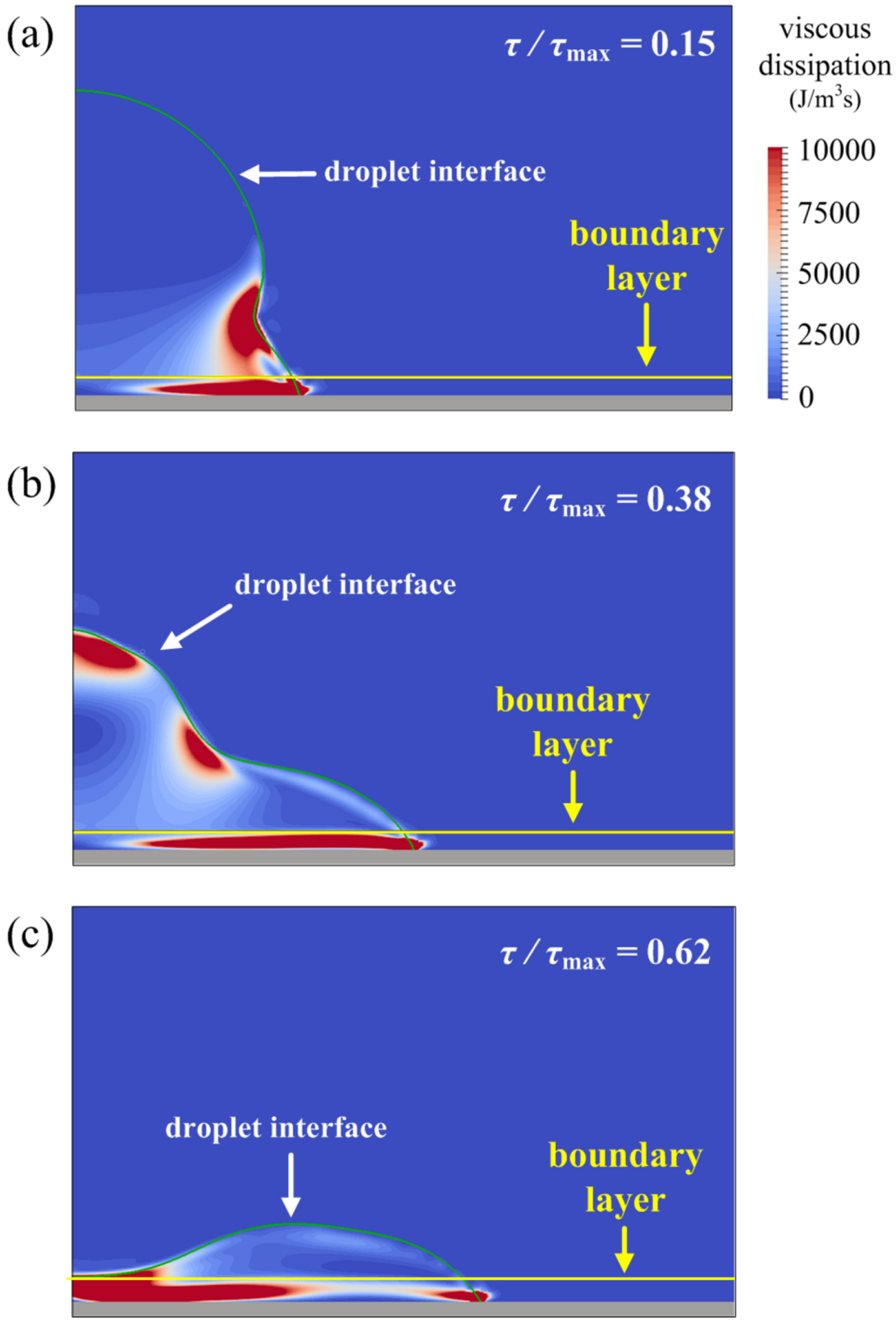

PLEASE CITE THIS ARTICLE AS DOI: 10.1063/5.0138378

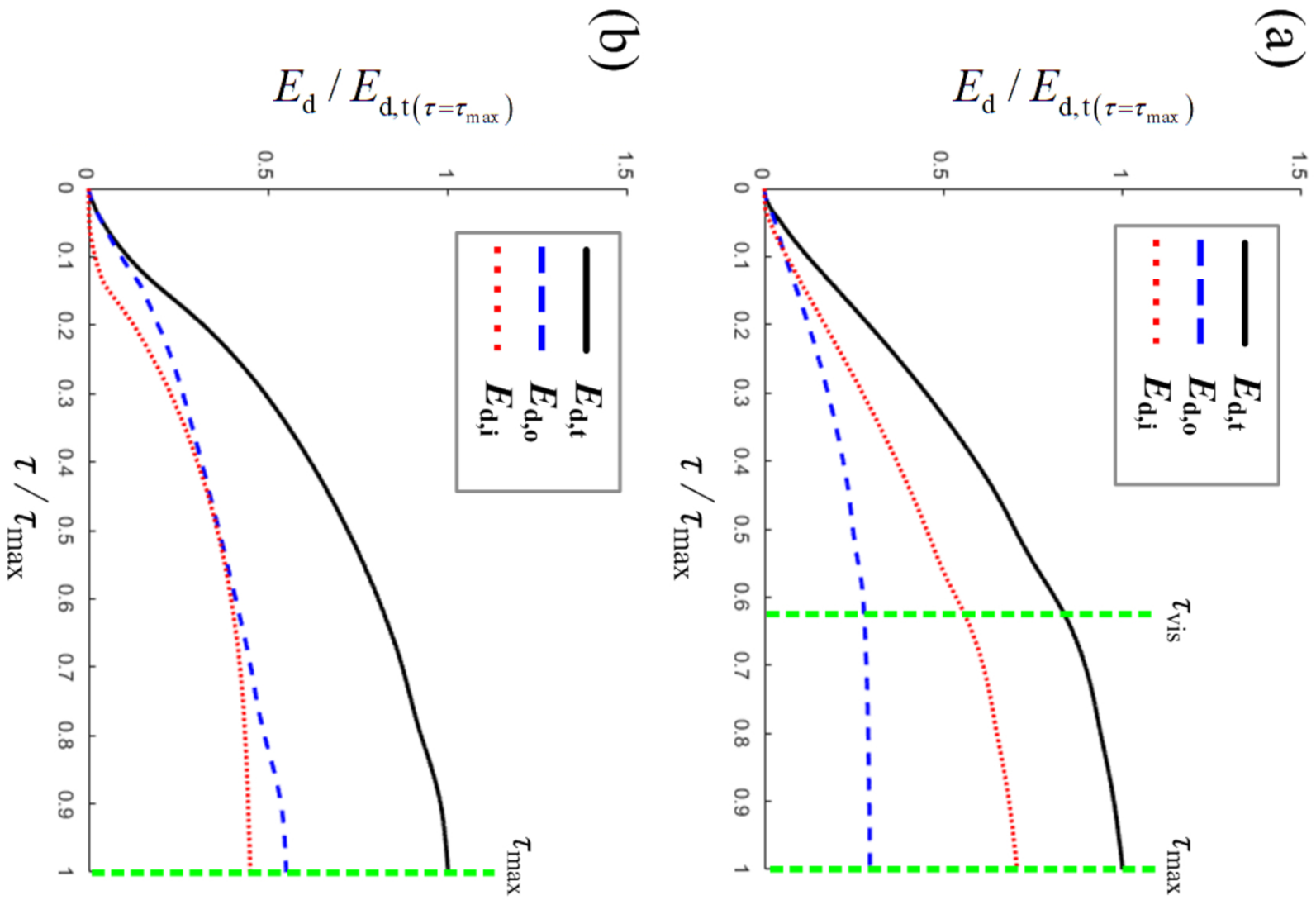

PLEASE CITE THIS ARTICLE AS DOI: 10.1063/5.0138378